RMetS
Royal Meteorological Society

Improving a spectral bin microphysical scheme using TRMM satellite observations

Xiaowen Li,[a,b]* Wei-Kuo Tao,[b] Toshihisa Matsui,[a,b] Chuntao Liu[c] and Hirohiko Masunaga[d]
[a]*Goddard Earth Science and Technology Center, University of Maryland, Baltimore, Maryland, USA*
[b]*Laboratory for Atmospheres, NASA Goddard Space Flight Center, Greenbelt, Maryland, USA*
[c]*Department of Meteorology, University of Utah, Salt Lake City, Utah, USA*
[d]*Hydrospheric Atmospheric Research Centre, Nagoya University, Nagoya, Japan*
*Correspondence to: Xiaowen Li, Code 613.1, NASA/GSFC, Greenbelt, MD 20770, USA. E-mail: xli@agnes.gsfc.nasa.gov

TRMM-observed mature-stage squall lines during late spring and early summer in the central USA over a 9-year period are compiled and compared with a case simulation by the Goddard Cumulus Ensemble (GCE) model with a spectral bin microphysical scheme. During the quasi-steady state of the simulation, a forward radiative transfer model calculates TRMM Precipitation Radar (PR) reflectivity and 85 GHz brightness temperatures from simulated particle size distributions. Comparisons between model and TRMM observations using radar Contoured Frequency with Altitude Diagrams (CFADs) and 85 GHz brightness temperature probability density distributions are performed, in addition to CFADs from a surface C-band radar for the same case. Radar CFADs comparisons reveal that the model overestimates sizes of snow/aggregates in the stratiform region.

Three sets of sensitivity tests are carried out in order to improve the simulated radar reflectivity profiles: increase of aggregates' density and terminal fall velocity; changing temperature dependency of collection efficiency between ice-phase particles, particularly those of the plate-type; and adding a break-up scheme for large aggregates. While all three approaches mitigate the discrepancies, changing collection efficiency produces the best match in magnitudes and characteristics of radar CFADs. In addition, interactions between ice- and water-phase particles also need to be adjusted in order to have good comparisons in both radar CFADs and 85 GHz brightness temperature distributions. This study shows that long-term satellite observations, especially those with multiple sensors, can be very useful in constraining model microphysics. Copyright © 2010 Royal Meteorological Society

Key Words: cloud-resolving model; squall line; microphysics

Received 21 April 2009; Revised 18 November 2009; Accepted 30 November 2009; Published online in Wiley InterScience 1 February 2010

Citation: Xiaowen L, Wei-Kuo T, Toshihisa M, Chuntao L, Hirohiko M, 2010. Improving a spectral bin microphysical scheme using TRMM satellite observations. *Q. J. R. Meteorol. Soc.* **136**: 382–399. DOI:10.1002/qj.569

1. Introduction

Proper representation of cloud and precipitation microphysics is one of the major challenges in cloud modelling and quantitative precipitation forecasting (e.g. Stoelinga *et al.*, 2003). Simple (one-moment) bulk microphysical schemes (e.g. Srivastava, 1967; Kessler, 1969; Cotton *et al.*, 1982; Lin *et al.*, 1983; Rutledge and Hobbs, 1984) have been used in cloud and mesoscale modelling for decades. There are numerous studies validating and improving bulk microphysical schemes (e.g. Tao and Simpson, 1989; McCumber *et al.*, 1991; Meyers *et al.*, 1992; Krueger *et al.*,

1995; Reisner *et al.*, 1998; Grabowski *et al.*, 1999; Luo *et al.*, 2003, 2008; Thompson *et al.*, 2004; Straka and Mansell, 2005; Lang *et al.*, 2007; Woods *et al.*, 2007; Zeng *et al.*, 2007). In addition to showing cloud models' large sensitivities to various microphysical parameters and processes, these studies indicated many limitations that are inherent in the simple bulk-type microphysical scheme.

With the advance of computer power, more sophisticated microphysical schemes have been developed/implemented in increasingly large modelling domains. These schemes generally fall into two categories: multiple-moment bulk schemes and spectral bin microphysical schemes. Multi-moment bulk schemes represent the particle size distributions (PSDs) better than the simple bulk scheme by using two or three, instead of only one, prognostic variables for each hydrometeor species (e.g. Cotton *et al.*, 1986; Murakami, 1990; Wang and Chang, 1993; Ferrier, 1994; Meyers *et al.*, 1997; Carrio and Nicolini, 2002; Chen and Liu, 2004; Morrison and Pinto, 2005; Milbrandt and Yau, 2005; Seifert and Beheng, 2006; Thompson *et al.*, 2008). However, they still have to make crucial assumptions on cloud droplet activation, pre-defined PSDs, as well as sedimentations of various particles. Spectral bin microphysical schemes use dozens, even hundreds of particle size bins to represent the actual size spectra of Cloud Condensation Nuclei (CCN) as well as different hydrometeor particles (e.g. Clark, 1973; Soong, 1974; Takahashi, 1975; Hall, 1980; Feingold *et al.*, 1994; Khain and Sednev, 1996; Reisin *et al.*, 1996; Geresdi, 1998; Ovtchinnikov and Kogan, 2000; Hashino and Tripoli, 2007). Cloud activation and PSD of various particles and their evolution are explicitly calculated in a bin model, making it an indispensable tool for studying detailed dynamics/microphysics interactions, such as aerosol indirect effects.

Unlike one-moment bulk microphysical schemes, which have gone through decades of validations for various cloud systems, the newly developed/implemented multi-moment bulk schemes and bin schemes have been subjected to relatively less systematic validation studies. In addition to traditional validation methods used for bulk microphysical models, these sophisticated schemes offer more depth in utilizing the wealth of observational datasets available (e.g. particle sizes and concentrations, ice-phase particle shapes, densities). This paper is the continuation of our previous studies (Li *et al.*, 2009) in validating a state-of-the-art bin microphysical scheme (Khain and Sednev, 1996; Khain *et al.*, 2000) that has been implemented in the Goddard Cumulus Ensemble (GCE) model (Tao and Simpson, 1993; Tao *et al.*, 2003). In the previous study, surface observations of the 10–11 June 1985 squall line during the Preliminary Regional Experiment for Storm-scale Operational and Research Meteorology (PRE-STORM) field campaign were used to validate both a bulk and the bin microphysical scheme in the GCE model. It was shown that the model simulations agreed well with the observed storm structure and evolution, radar reflectivity patterns, wind fields, retrieved pressure and temperature perturbations, as well as heating profiles. This study further includes nine years of Tropical Rainfall Measurement Mission (TRMM) satellite data, in addition to some surface radar observations during the PRE-STORM field campaign, to validate and improve the model microphysics.

Several previous studies have used TRMM data for validating cloud models. For example, Zhou *et al.* (2007) uses TRMM retrievals during the South China Sea Monsoon Experiment (SCSMEX) to validate GCE model simulation. The TRMM Microwave Imager (TMI) observed brightness temperatures have also been used in several model validations (e.g. Wiedner *et al.*, 2004; Lang *et al.*, 2007; Li *et al.*, 2008). Li *et al.* (2008) further included TRMM Precipitation Radar (PR) 20 dBZ and 40 dBZ maximum heights in their validation of a tropical oceanic mesoscale convective system simulation. More recently, Matsui *et al.* (2009) established a systematic radiance-based evaluation using multi-sensor satellite simulators and TRMM PR, TMI, as well as the Visible and InfraRed Scanner (VIRS) to validate long-term GCE simulations of both SCSMEX and Kwajalein Experiment (KWAJEX) field campaigns. Masunaga *et al.* (2008) also used both TRMM PR and CloudSat radar reflectivity to evaluate the macro- and micro-properties of a global cloud-resolving model simulation of the Madden–Julian Oscillation.

This study is the first in attempting radiance-based model validation and improvement using a sophisticated bin microphysical scheme. Compared to bulk scheme validations, bin scheme validations offer both advantages and new challenges. Because PSDs are explicitly calculated in bin models, one major uncertainty associated with the PSD assumptions in either satellite retrieval or forward radiative transfer calculation is eliminated. Improvements made in bin schemes will be based more on fundamentals, without the need to adjust PSDs, especially for ice-phase particles with many uncertainties. On the other hand, improving bin schemes according to satellite observation requires clear understanding of the myriad of interlacing microphysical processes. It also inevitably involves uncertainties as bin schemes have more degrees of freedom than available observational constraints. Another issue is computational. Bulk scheme models can potentially afford better match between satellite and model data through long-term simulations over large, three-dimensional (3D) domains. On the other hand, our bin scheme simulation is a 2D, 12-hour-period case-study which necessitates careful comparisons between specific features, as discussed in detail in section 2.1.

The paper is organized as follows. The second section briefly describes the PRE-STORM case, the GCE model with bin microphysical scheme, and the forward radiative transfer calculations. The third section analyses and compares TRMM and C-band surface radar data with each other, and with model simulations. Section 4 includes diagnostic studies using the GCE model, the resultant improvements in the bin microphysical scheme, and comparisons between the improved model and observations. A summary and discussion are given in section 5.

2. Descriptions

2.1. PRE-STORM case

The PRE-STORM 10–11 June 1985 case is a well-studied midlatitude continental squall-line case (e.g. Rutledge *et al.*, 1988; Johnson and Hamilton, 1988; Zhang *et al.*, 1989; Gallus and Johnson, 1991; Biggerstaff and Houze, 1993; Tao *et al.*, 1993, 1995, 1996; Braun and Houze, 1996). It is a typical squall system travelling from northwest to southeast during late spring and early summer in the central USA. Figure 1, which is a schematic plot of the cross-section of this type of system, depicts the main microphysical processes associated with particle formation and growth (adapted from Houze, 1989). The 'convective region' shown in Figure 1 has a width

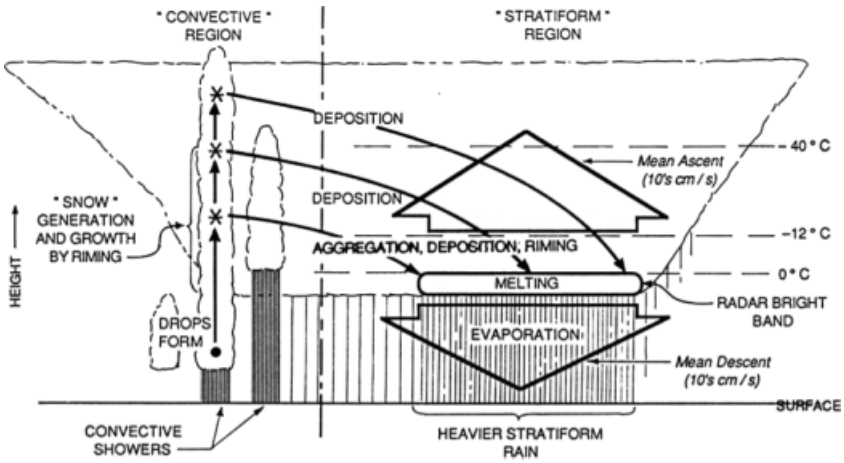

Figure 1. Schematic plot of a typical squall line. Copied from Fig. 2 in Houze (1989).

of 20–30 km. The trailing 'stratiform region' can extend to more than 100 km. Several reasons make this type of precipitation system ideal for evaluating our bin scheme cloud-resolving model using TRMM satellite observations:

- First of all, both the coverage and resolution of the TRMM satellite are suitable for observing large squall systems. The TMI conical scanning has a swath of 878 km (after the satellite orbit boost in August 2001, and slightly narrower before that), which is large enough to capture a typical squall system within its overpass. PR has a narrower swath of 247 km (after the orbit boost), which is marginal for covering a squall system. But the 5 km footprint of TRMM PR with 0.25 km vertical resolution offers excellent sampling, especially in the homogeneous stratiform region, which is the emphasis of this study.
- Secondly, squall lines are long-lived systems with a quasi-steady mature stage that lasts from several to more than ten hours. The mature stage of a squall line has very robust structures, which are exploited in this study to expand the satellite dataset and provide good statistics. In addition, the mature stage is well captured by idealized cloud-resolving model simulations. In this study, we compare only the mature stage of the squall line, which takes out the many uncertainties associated with an individual cloud's life cycle, as well as the impact of a 'cold' start (i.e. cool pool initialization) in our simulation.
- Thirdly, the extensive, homogeneous stratiform region offers an ideal test-bed for ice-phase microphysical processes. As shown in Figure 1, the ice hydrometeors generated in the deep convection are advected back to the stratiform region, where they further grow by deposition, aggregation, and less frequently, by riming while falling through a deep layer of weak ascending motion of ∼10 cm/s. In our simulation, there is very little liquid water in the stratiform region. Ice-phase particle growth in the stratiform region involves exclusively deposition and aggregation/splintering. These provide very useful constraints when improving the model ice-phase microphysics.
- Lastly, a squall line has a quasi-2D structure as shown in Figure 1. The general structure illustrated in Figure 1 repeats itself along a line ranging from tens of kilometres to hundreds of kilometres in length. This type of linear structure can be realistically captured with a computationally efficient 2D model as used in this study (i.e. Weisman *et al.*, 1988; Fovell and Dailey, 1995; Parker and Johnson, 2004). However, 3D simulations are still required in order to simulate asymmetrical development of squall lines, e.g. a squall line with right-flank supercells (Dudhia and Moncrieff, 1989). Furthermore, Cotton *et al.* (1995) suggested that a 2D framework cannot simulate the cross-squall flow of mid-level air that is evident in their 3D simulation.

2.2. *Model description*

The 2D anelastic version of the GCE model coupled with the spectral bin microphysical scheme from the Hebrew University Cloud Model (HUCM) are used in simulating the PRE-STORM squall-line case. The model is initialized with a single sounding taken ahead of the forming squall line. A low-level cool pool is applied for the first 10 minutes to initialize convection (e.g. Tao *et al.*, 1991; Trier *et al.*, 1996). The horizontal resolution is 1 km with stretched, open lateral boundaries. No large-scale advection of water vapour or heat is imposed in this case simulation. There are 33 stretched vertical levels with a resolution of 240 m at the lowest level and 1250 m at the top. The total integration time is 12 hours with $\Delta t = 6$ s. The model achieves a quasi-steady state with cloud structure similar to Figure 1 after about 6 hours. Only the quasi-steady-state data (6 to 12 hours in our simulation) are used in this study. For detailed descriptions of storm evolution and structure, the readers are referred to Li *et al.* (2009).

The HUCM bin microphysical scheme explicitly simulates size spectra of seven hydrometeor types: cloud/rain, three types of ice crystals (plate, column and dendrite), snow/aggregates, graupel, hail/frozen drops, as well as Cloud Condensation Nuclei (CCN). There are 33 size bins representing each species' size spectrum. Both cloud and ice nucleation, diffusional growth of water and ice phase, drop–drop, drop–ice, and ice–ice collision/coalescence, ice multiplication, collisional break-up of raindrops, freezing, and melting are represented explicitly in this model. Details of the HUCM bin scheme can be found in Khain and Sednev (1996) and Khain *et al.* (2000, 2004).

2.3. Forward radiative transfer calculations

For comparing direct satellite observations with model simulations, one needs to use a forward radiative transfer model to calculate the observed satellite signals using simulated hydrometeor profiles and size distributions. The Goddard Satellite Data Simulation Unit (SDSU: Matsui *et al.*, 2009) is used in this study. The SDSU simulates satellite-consistent radiances or backscattering using GCE model output. Currently, there are simulators for passive microwave, radar, passive visible–infrared, Lidar, broadband short-wave and long-wave, as well as ISCCP-like (International Satellite Cloud Climatology Project) observations within the unit. Here we use the passive microwave and radar simulators. The 85 GHz TMI brightness temperatures (BTs) are simulated using delta-Eddington two-stream radiative transfer with slant path view (Kummerow, 1993; Olson and Kummerow, 1996). The 14 GHz TRMM PR reflectivity is calculated according to Masunaga and Kummerow (2005). A derivation of the radar equation is also given in detail in Masunaga and Kummerow (2005). For both the passive microwave and active radar simulator, the electromagnetic properties of simulated hydrometeor profiles are calculated via Mie theory (spherical assumption). The dielectric function of a melting particle uses the Maxwell–Garnet formula (e.g. Bohren and Battan, 1980). Simulated BTs and radar reflectivity are convolved within the TRMM instruments' instantaneous field of view through a Gaussian beam pattern. TRMM PR data used in this study are attenuation-corrected. Therefore SDSU does not include attenuation in radar reflectivity calculations. Surface emissivity for TMI simulation uses the average value within the same data box during August 2006 TRMM observations (Karbou, 2008). The upward pointing surface C-band radar reflectivity is simulated using the same radar simulator, but at the corresponding wavelength of 5.5 cm and surface operating mode.

3. Model evaluation

3.1. Data

Two sets of data are used for model evaluation: two time frames of gridded ground-based C-band radar data during the mature stage of the PRE-STORM experiment, and the nine years of TRMM satellite observations (1998–2006) of the squall lines over southern central USA.

3.1.1. Surface radar

Figure 2 shows radar reflectivity measured by the C-band radar at 01:39:00 and 03:44:59 UTC on 11 June 1985, during the mature stage of the PRE-STORM squall line. Figure 2(a) catches the whole system with a bowed leading edge and a stratiform region extending more than 100 km in width. Figure 2(b) shows only the stratiform region of the same system more than two hours later. The leading edge is again to the right of the system. The vertical cross-section along the black line in Figure 2(a) is plotted in Figure 2(c), which closely resembles the schematic plot shown in Figure 1, as well as the simulated radar reflectivity during the mature stage, as shown in Figure 2(h). The Contoured Frequency with Altitude Diagrams (CFADs: Yuter and Houze, 1995) are used for quantitative comparisons between observations by radar and model simulations. The CFADs represent frequency distributions at each height for the 3D radar observations, as shown in Figure 2(e), (f) and (g). Figure 2(e) and (f) are for the stratiform and convective region in Figure 2(a), respectively. The stratiform CFADs at both time frames show similar features. Above the melting level, the radar reflectivity shows remarkable homogeneity. The vast majority of the data points cluster within a narrow band of ± 3 dBZ, which decreases from about 25 dBZ right above the melting band to10 dBZ at about 11 km. The CFADs have more scatter below the melting band, but still show the majority of data points between 25 to 35 dBZ, with a slight trend of decreasing intensity with decreasing height. The convective region CFADs, on the other hand, have much wider scatter, about 20 dBZ, throughout different heights as shown in Figure 2(f). Although CFADs in the convective region can provide some qualitative information when used for model validation, the uncertainty becomes much larger compared with using stratiform CFADs. For this reason, we concentrate on analysing radar CFADs for the stratiform region only. Another reason for using only the stratiform region is that TRMM PR has a marginal resolution in detecting single convective cores, which when used, adds another degree of uncertainty to model validation.

3.1.2. TRMM data

The TRMM satellite carries a suite of sensors for rainfall measurement. We use the two major quantitative rainfall measure sensors: the microwave imager TMI, and the Ku-band Precipitation Radar. As stated in section 1, only direct measurements are used for model validation. For PR, we use attenuation-corrected radar reflectivity. For TMI, we use 85 GHz Polarization Corrected Temperature (PCT) defined as $PCT = (\beta T_{\mathrm{BH}} - T_{\mathrm{BV}})/(\beta - 1)$, where β has a fixed value of 0.45 according to Spencer *et al.* (1989), and T_{BH} and T_{BV} are horizontally and vertically polarized brightness temperatures. Other TRMM rainfall measurements are investigated, but they turn out to be either heavily contaminated by surface emission (e.g. 37 GHz BT over land), or too noisy (e.g. the PR path-integrated attenuation in the stratiform region) to be used confidently for model validation.

This study takes advantage of the University of Utah TRMM precipitation feature database (Nesbitt *et al.*, 2000; Liu *et al.*, 2008). The first step is to identify squall lines similar to the PRE-STORM case at the same geographic location around the same time over nine years of TRMM measurements. Figure 3 shows our study region that is enclosed by the dashed lines (90°W–103°W, 31°N–39.5°N). It encompasses the southern Great Plains and the central plain that are between the Rocky Mountains and the Appalachians. Previous studies (e.g. Velasco and Fritsch, 1987) show that this is the area where most of the mesoscale convective complexes occur. Also, the location of these mesoscale convective complexes tends to be over the southern plains during late spring and moves up north in late summer/early autumn. Our northern edge is confined by TRMM TMI's range to about 40°N. TRMM PR has a narrower range (up to 36°N) that is represented by the thin solid line. The southern edge is chosen so that coastlines and local convection triggered by the coastal circulations can be avoided. The shaded area in Figure 3 covers the PRE-STORM squall-line track over its 9-hour development (2300 UTC 10

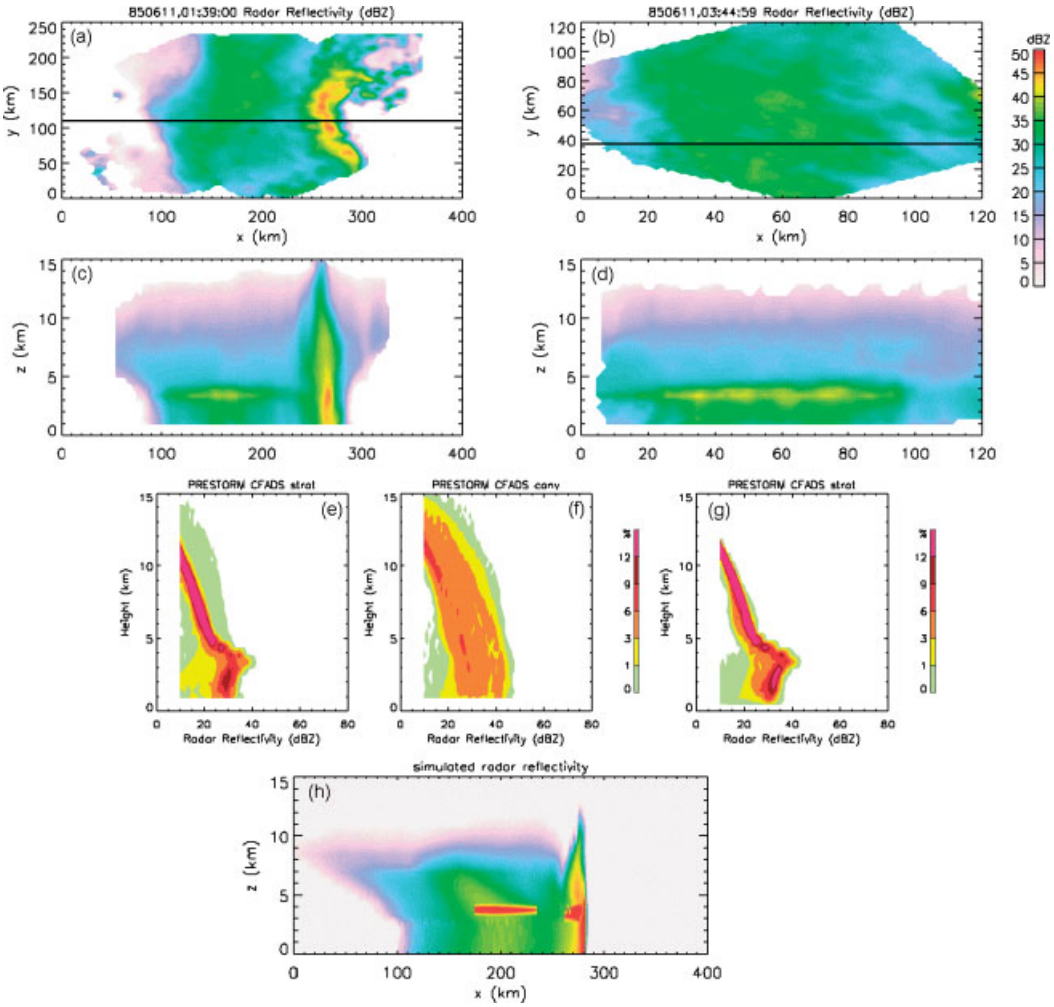

Figure 2. C-band surface radar observations during PRE-STORM and comparison with model simulation. (a) Surface radar reflectivity at 01:39:00 UTC 11 June 1985; (b) Same as (a) except at 03:44:59 UTC; (c) radar reflectivity cross-section along the black line in (a); (d) radar reflectivity cross-section along the black line in (b); (e) radar CFAD for the stratiform region in (a); (f) radar CFAD for the convective region in (a); (g) radar CFAD for the stratiform region in (b); (h) radar reflectivity simulated by 2D GCE model at $t = 12$ hours. (Radar data courtesy of Robert A. Houze Jr and Jasmine Cetrone at University of Washington, Seattle).

June to 0800 UTC 11 June 1985). All mesoscale convective systems as defined in the University of Utah database during late spring and early summer (1 May–31 July) over the 9-year period are visually examined to identify squall lines. Only TMI images are used for system identification because of their good coverage. Convection is defined when the 85 GHz PCT of a system is below 180 K. To qualify as a squall line, a continuous band of convection has to be at least 100 km in length and has a length-to-width ratio of at least 4. Among over 500 mesoscale convective system cases in the database, 51 cases are identified as squall lines. Since our study uses only the mature stage simulations with a significant stratiform region, we further require the total width of the identified squall line to be at least 3 times the width of its convective line. Using these criteria, a total of 41 squall lines have a significant stratiform region. These 41 cases form the base of the TMI brightness temperature evaluation.

Figure 4 shows three examples of TRMM-observed squall lines. They include two basic types: the symmetric (the first two columns) and the asymmetric (the third column) (Houze, *et al.*, 1990). The symmetric system has an evenly distributed convective line with new cells regenerating ahead of its leading edge. The stratiform region has its centre

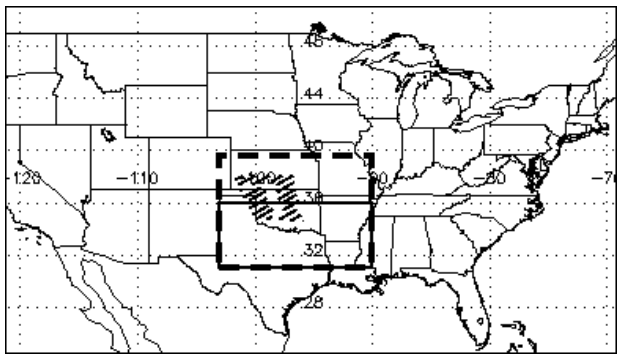

Figure 3. US map with dashed-line frame representing the TMI data range, and the solid-line frame within it, the PR data range. The shaded area is the propagation track of the PRE-STORM squall-line case over its 9-hour evolution.

directly behind the convective line. The asymmetric system has stronger, newly developed convection at one end (the southwest) and weaker, dissipating convection at the other end. The centre of its stratiform region is also biased toward the northeast – the weaker convection end. Among the 41 cases identified as mature-stage squall lines, 32 are symmetric and 9 are asymmetric. The PRE-STORM case

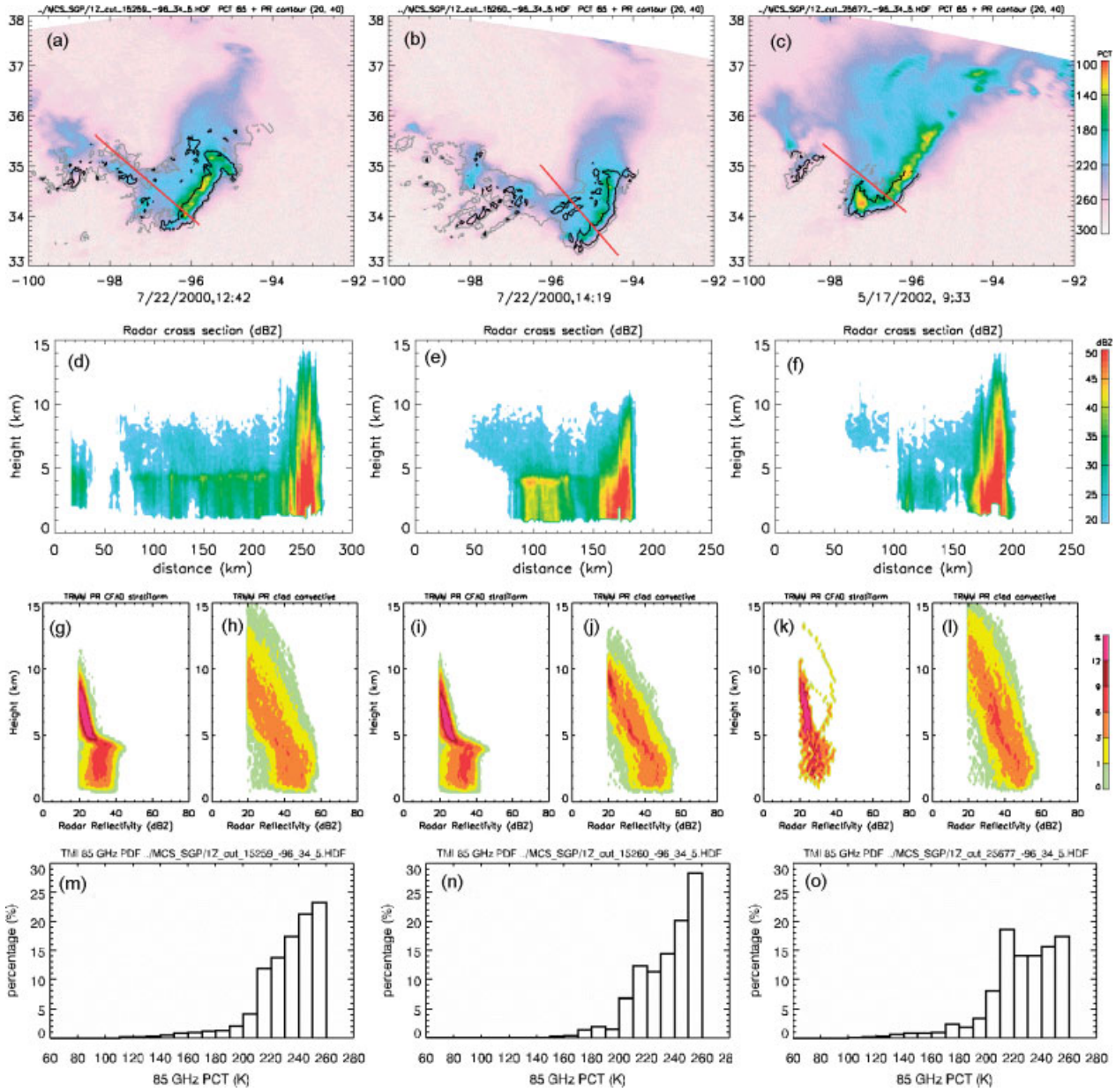

Figure 4. Three examples of TRMM-observed squall lines over the area described in Figure 3. Each column represents one case. The first row (a)–(c) shows images of 85 GHz PCT with 40 dBZ (black lines) and 20 dBZ (grey line) surface radar reflectivity overlaid. The second row (d)–(f) is the corresponding radar reflectivity cross-sections along the red lines in the first row. The third row (g)–(l) shows radar reflectivity CFADs for each case. The stratiform CFADs are on the left-hand side and the convective CFADs are on the right-hand side. The fourth row (m)–(o) is the probability density distributions of 85 GHz PCT, binned in 10 K intervals, for the whole system without distinguishing convective and stratiform.

shown in Figure 2(a) is a symmetric system. However, as far as the cross-section of a squall is concerned, which is most relevant to 2D model simulations, both types of squall line have the same structure as shown in Figure 1. This is the reason that we include the 9 asymmetric systems in our comparison. PR stratiform CFADs show little differences between the symmetric and asymmetric systems. The TMI probability density distributions in asymmetric systems have a flatter tail at the high-BT end compared with symmetric cases (cf. Figure 4(m), (n) and (o)). But the difference does not affect the ensemble of probability density functions used in our comparison study.

The first two columns in Figure 4 are the same system observed at different times. Figure 4(a) and (b) are about an hour and a half apart and demonstrate the steady development of a mature squall line. The first row in Figure 4 shows images of 85 GHz PCT with the 40 dBZ PR surface reflectivity overlaid as black contours and the 20 dBZ as grey contours. The radar has excellent coverage for these two cases. Radar reflectivity cross-sections along the red lines in Figure 4(a), (b) and (c) are shown in the second row. One can clearly see the resemblance between these radar images and the C-band radar observation in Figure 2, as well as the schematic plot in Figure 1. CFADs of radar reflectivity are plotted in the third row, again separated by stratiform and convective region. The stratiform region is defined as rain-type flag equal to 100 (stratiform identified by both vertical profile and horizontal pattern) in TRMM version 6 product 2A23. All convective-certain flags (200, 210 and 220) are used for convective CFADs plots. Since a squall line has a very clear-cut separation between the convective and stratiform regions, CFADs plots are not sensitive to different definitions of convective and stratiform types in either the TRMM product or model separation methods. Similar to

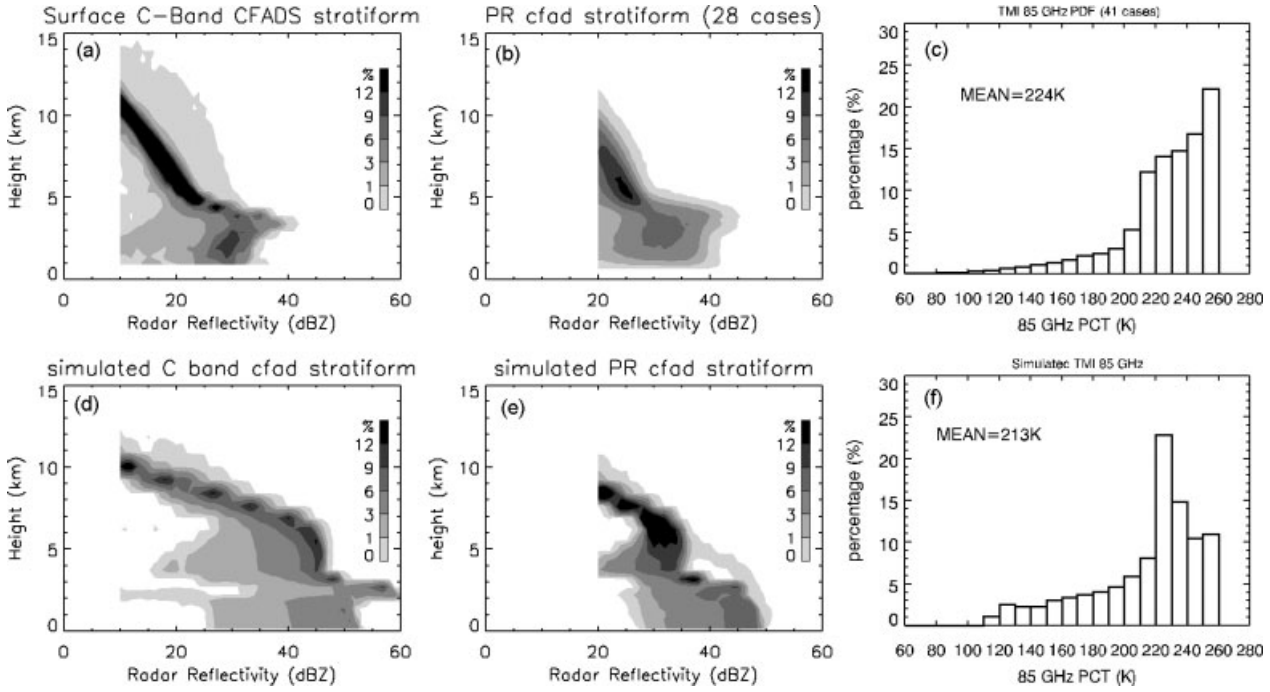

Figure 5. Comparisons between observations (upper row) and model simulations (lower row). (a) Surface C-band radar CFAD in stratiform region at 01:39:00 UTC 11 June 1985; (b) TRMM PR CFAD in stratiform region for 28 squall-line cases over 9 years; (c) TRMM TMI 85 GHz PCT probability density distribution for 41 squall-line cases; (d) simulated C-band radar CFAD in stratiform region during the mature stage of the PRE-STORM case-study; (e) same as (d) except for the TRMM PR frequency and field of view; (f) simulated TRMM TMI 85 GHz PCT probability density distribution during the mature stage of the system.

surface C-band radar in Figure 2, stratiform CFADs in Figure 4 show very narrow distributions and consistent features for all three cases. In contrast, significantly more variations are seen in convective CFADs. The probability density distributions of 85 GHz PCT are plotted in the fourth row of Figure 4(m), (n) and (o). The PCTs are binned in 10 K intervals and the highest value is cut at 260 K to avoid excessive surface contamination. Since the microwave imager does not provide enough information to separate convective from stratiform regions, the plots are for the whole system. Despite variations in detailed distributions for each case, several characteristics show up consistently. First, the vast majority of the data points lie above 200 K. Even for a system as strong as the asymmetric case, only less than 10% of data are below 200 K. Second, the PCT distributions are not smooth, in that there is a large jump in the distributions between 200 and 220 K. This is very consistent behaviour for all the mature-stage squall lines in this study, as will be shown in the next section.

The asymmetric case in Figure 4(c) also represents a situation with limited PR coverage. Since PR has a much narrower swath than TMI, only 28 out of the 41 identified mature squall lines have some radar coverage in the stratiform region and are used for compiling the stratiform radar reflectivity CFADs. Figure 4(c) represents the borderline stratiform coverage. Any case with radar coverage less than this is rejected. One can see that the stratiform CFADs in Figure 4(k) are blotchy compared with Figure 4(g) and (i) because of their limited data size, although the main features remain consistent. The outlier bands above 5 km in the stratiform CFAD plot are produced by the small rain area to the west of the main system, which might be remnants of earlier convection. The 'hook' at the south end of this squall line has the strongest convection; such hooks are often associated with strong surface winds and tornados (e.g. Fujita, 1981; Weisman, 1993).

3.2. *Comparisons*

Radar reflectivity CFADs comparisons among surface radar, TRMM PR and simulated reflectivity are shown in Figure 5. The lowest reflectivity is cut at 10 dBZ for the C-band radar and 20 dBZ for PR according to their sensitivities. As discussed in the previous section, only the stratiform region radar data are used for model evaluations. Figure 5(a) is the radar reflectivity CFADs at 01:39:00 UTC 11 June 1985. Figure 5(d) is the simulated C-band radar reflectivity during the mature stage of the simulation (6–12 hours) with output every 5 minutes. All seven hydrometeor types in the bin model are included for the forward radiative transfer calculation. Figure 5(b) is the composite of stratiform reflectivity CFADs of all 28 identified cases with stratiform PR coverage, and Figure 5(e) is the simulations using the same hydrometeor outputs as in Figure 5(d), except at PR frequency of 13.8 GHz.

Despite the fact that Figure 5(b) is the composite of 28 different cases over a 9-year period, it shows good consistency and the same features as a single squall line (cf. Figure 4(g), (i) and (k)). This confirms the robust structure in the homogeneous stratiform region. For example, radar reflectivity remains below 30 dBZ above the melting level in Figure 5(b), and decreases roughly linearly down to 20 dBZ at around 9 km. C-band radar CFADs in Figure 5(a) show similar features, but are slightly weaker than the TRMM composite.

Model simulations obviously overestimate radar reflectivity compared with both surface C-band radar (Figure 5(d)) and PR (Figure 5(e)). Surface radar reflectivity is more than 10 dBZ higher at both frequencies. Above the melting level,

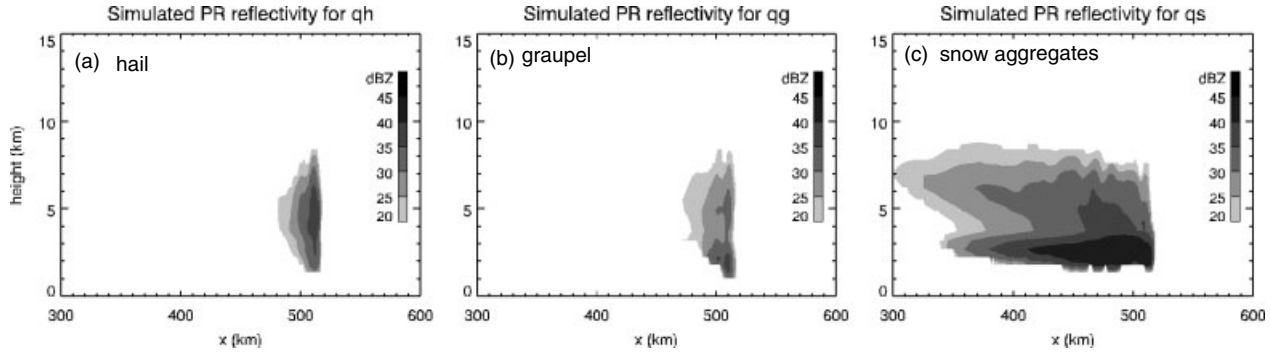

Figure 6. Simulated PR reflectivity for single ice-phase species: (a) hail; (b) graupel; and (c) snow aggregates, at the end of the 12-hour simulation.

for ice-phase particles, radar reflectivity remains more than 10 dBZ higher at C-band. The differences between simulations and TRMM PR observations are about 5 dBZ. Between 4 km and 7 km, simulated radar reflectivity profiles stay more or less vertical, indicating almost constant reflectivity in this region, in contrast to the linear increasing trend observed in both C-band and PR. Above 7 km, both Figure 5(d) and (e) have more rapid linear decrease, which ultimately lead to a reasonable radar reflectivity range at around 10 km compared with observations.

The simulated 85 GHz TMI PCT compares reasonably well with TRMM observations, as shown in Figure 5(c) and (f). Figure 5(c) is the composite of probability density distributions for all 41 cases. As with single cases in Figure 4, one finds a clear jump of frequency of occurrence at around 220 K. The simulation also shows a nice match of the jump at around 220 K. However, its frequencies below 200 K PCT have higher values than the observations. After the jump, the frequencies taper down instead of increasing continuously as in Figure 5(c). As a result, the mean simulated 85 GHz PCT is about 11 K lower than the TRMM composite. However, some of these differences can be attributed to the 2D geometry used in the simulation, where there is only one edge area (with relatively high BT) in the stratiform region, compared with three in a realistic 3D situation. This can also be seen from comparing Figure 4(o) to Figure 4(m) and (n). In the asymmetric system in Figure 4(o), the edge area is smaller compared with the symmetric system in Figure 4(m) and (n), and thus the tapering off of the PCT distribution at the high-value tail.

4. Bin microphysical scheme improvements

The comparison between observations and model simulations in Figure 5 shows large discrepancies in radar reflectivity profiles. This clearly indicates the need for improvements in model simulations. There are many uncertainties inherent in the cloud model simulations, ranging from numerical errors to physical uncertainties. Since previous studies of the same case (Li *et al.*, 2009) show good comparisons in model kinematics and dynamics, here we focus on analysing uncertainties in the bin microphysical scheme itself, which is most relevant and sensitive to the TRMM satellite observations. Even within microphysics, solutions are far from unique based on the limited constraints provided by observations. Our approach to this problem is that, with a clear physical understanding, we will do the *least* possible amount of adjustment in processes/parameters to improve the comparisons.

4.1. *Diagnoses*

Figure 5(d) and (e) indicate high concentrations of large raindrops simulated by the model near the surface, which produce more than 10 dBZ overestimation of surface radar reflectivity on average. Since rainfall rates in the stratiform region are generally below 6 mm/h, the raindrop collision/coalescence process plays a relatively small role in shaping its size distribution. The simulated large raindrops mainly come from melted large ice-phase particles, as indicated by large radar reflectivity above the melting level. In order to identify the source(s) of large ice-phase particles, Figure 6 shows simulated radar reflectivity of single ice-phase species at $t = 12$ hours. It is readily seen that both hail and graupel are confined mainly to the convective region and the transitional zone immediately behind it. Snow aggregates are by far the dominant species contributing to radar reflectivity signals in the upper stratiform region. Pristine crystals are not shown because they contribute very little to the total PR signal, although they are still included when calculating the total simulated radar reflectivity.

The main source of stratiform ice-phase particles is the detrainment from leading convection. These detrained particles further grow by deposition and aggregation in the stratiform region until they reach the melting level, as illustrated in Figure 1. Since growth by deposition is limited by the mean updraught, which compares well with observations (Li *et al.*, 2009), one concludes that growth by aggregation should be overestimated, especially at upper levels. As shown in Figure 5(d) and (e), simulated radar reflectivity increases much faster with decreasing height compared with the corresponding observations until about 6 km. At that point, snow aggregates become so large that the differences of their fall velocities start diminishing because the terminal fall velocity of snow aggregates approaches a constant value as their sizes increase. This prevents further increases of the mean particle size by aggregation. From 6 km to around 4 km, simulated radar reflectivity remains roughly constant, which is not observed in either ground or spaceborne radar.

4.2. *Improvements*

Growth rates of snow aggregates by collection are represented by the stochastic collection equation (e.g.

Pruppacher and Klett, 1997) in the bin scheme:

$$\frac{\mathrm{d}n_k}{\mathrm{d}t} = \frac{1}{2} \int_0^{m_k=m_i+m_j} K_{k-j,j} n_{k-j} n_j \mathrm{d}m_j - n_k \int_0^{\infty} K_{kj} n_j \mathrm{d}m_j,$$

where n_k is the number concentration of particles with mass m_k; K_{ij} is the collection kernel of two particles with mass m_i and m_j. Assuming a geometric sweep-out kernel:

$$K_{ij} = \frac{\pi}{4} \left(D_i + D_j\right)^2 \left|v_i - v_j\right| E_c,$$

where D_i and v_i are the diameter and terminal fall velocity of an ice particle with mass m_i. E_c is the collection efficiency, which itself depends on temperature, humidity, shapes and sizes of various ice particles. There are many uncertainties associated with each variable in K_{ij}. For example, densities of snow aggregates vary by a factor of more than 2 in different measurements (e.g. Mitchell, 1994; Brandes *et al.*, 2007). Terminal fall velocity of various ice-phase particles can be determined either by observations (e.g. Locatelli and Hobbs, 1974; Heymsfield, 2003; Brandes *et al.*, 2008) or numerical calculations (e.g. Böhm, 1989; Mitchell and Heymsfield, 2005) and the results also vary by several factors. In addition, irregular ice particles tumble along their falling path, with oscillating fall velocities.

Collection efficiency E_c is by far the most uncertain factor in collection kernel K_{ij}. While uncertainties in densities and terminal fall velocities are generally within several-fold, E_c measurements vary by orders of magnitudes. Figure 7 shows examples of both measurements and model specifications for $E_c(T)$. The grey boxes are values of E_c from various laboratory experiments, summarized in Pruppacher and Klett (1997), fig. 14–18. Note these experiments were done in the 1960s and 1970s and most of them used ice spheres as collectors. Temperatures in these experiments are also relatively warm. Airborne image sensors were later used to derive E_c. Some studies used statistics of the images (e.g. Kajikawa and Heymsfield, 1989), others used co-ordinated flight paths and aggregation models (e.g. Passarelli, 1978; Field and Heymsfield, 2003; Field *et al.*, 2006). Even using the same method, the measured E_c still vary by magnitudes in some cases, as shown in Figure 7. Apparently more basic research is needed to determine these collection efficiencies.

With such a wide range in E_c values, more sophisticated models (two-moment, bin spectral) used *in situ* observations to try to constrain it. Figure 7 lists some results of these models. Cotton *et al.* (1986) experimented with E_c formulations using an exponential fit from laboratory measurements by Hallgren and Hosler (1960) (dash-dotted line in Figure 7) and aircraft observations by Passarelli (1978) in a cloud-resolving model and compared their results to surface observations. Mitchell (1988) used comparisons between his snow growth model and aircraft observations and decided on $E_c = 0.1$ for all species when relative humidity is below water saturation. When relative humidity is above water saturation, E_c varied between 0.1 and 1 depending on temperature and shapes of particles. Again, there is no consensus in model simulations.

There is observational evidence that E_c also depends on relative humidity (e.g. Hosler *et al.*, 1957), but very little quantitative information is available. In our model, E_c varies linearly with relative humidity with respect to ice. Sensitivity tests (not plotted) on E_c variations with relative humidity (RH) do not improve comparisons, therefore the original formulation is retained. Future laboratory studies are needed to resolve this issue. The temperature dependence of E_c in our original scheme is plotted in Figure 7 as the dashed line. They are the combinations of fitting and extrapolations of measurements (Khain and Sednev, 1996). The bump-up of E_c between -17°C and -12°C represents the observed high aggregation level due to dendrite formations (e.g. Ohtake, 1970; Passarelli, 1978). Note this E_c value has been applied to aggregational growth of all ice species with different shapes, which is a questionable assumption and needs further study.

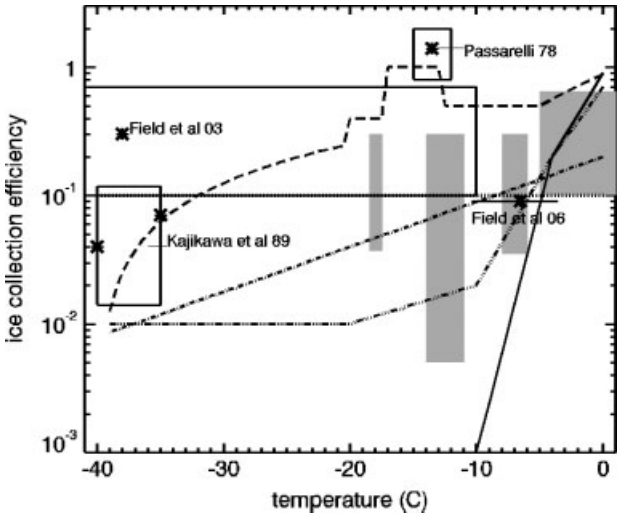

Figure 7. Ice particle collection efficiency vs. temperature. The grey boxes indicate ranges of Pruppacher and Klett (1997)'s summary of laboratory measurements. Boxes and lines with asterisks in/on them are derived from aircraft measurements. Each box represents the ranges of one particular measurement and each asterisk represents the mean value. The lines are the collection efficiencies used in various cloud models (either bin spectral or two-moment) that specifically compared modelled ice particle sizes with observations: the dashed line is the original curve used in the spectral bin scheme in the GCE model; the solid line is the revised curve that improves radar reflectivity comparison in experiment 'Ec'; the dash-dot-dot-dot line is used in experiment 'graup' where both radar reflectivity and 85 GHz PCT compare well with observations. The dotted line ($E_c = 0.1$) and the dash-dotted line are from two other model simulations: one is Mitchell (1988), the other is Cotton *et al.* (1986).

Previous discussions focus on source terms of large snow aggregates. Alternatively, it is possible to add a sink term in the aggregates' growth equation. Since radar reflectivity is proportional to the sixth power of particle diameter, very large snow aggregates dominate radar signals. Assuming these large particles are unstable, they may break up spontaneously or upon collision with other particles, thus produce lower radar reflectivity. This process is not considered in the original bin microphysical scheme.

Many sensitivity tests are performed in order to reduce discrepancies between radar observations and model simulations. We present here three independent approaches. Experiment 'rho_vt' increases bulk densities of large snow aggregates and their terminal fall velocities within their uncertainty ranges. Experiment 'Ec' reduces ice-phase particles' collection kernel by modifying temperature dependency on collection efficiency E_c. Experiment 'sbreakup' adds a simple break-up scheme for large snow aggregates to reduce their mass density.

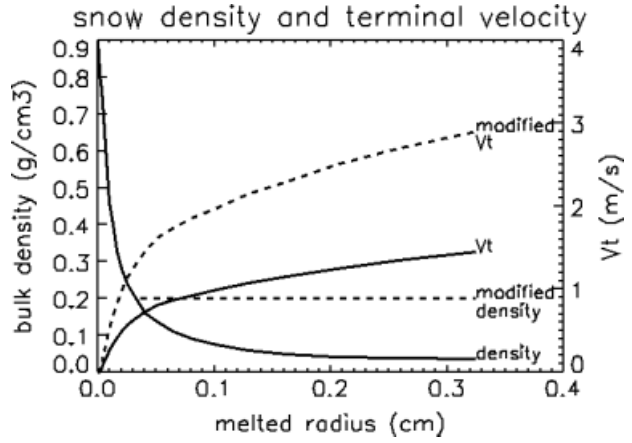

Figure 8. Bulk densities and terminal fall velocities of snow aggregates used in the bin microphysical scheme. The radius along the *x*-axis is the equivalent drop radius of a melted particle. Bulk densities decrease with size while terminal velocities increase with size. The solid lines are the values used in the original bin scheme, while the dashed lines are the modified values in sensitivity experiment 'rho_vt'.

4.2.1. *Bulk density and terminal fall velocity*

Several model simulations have been carried out where snow aggregates' densities and/or their fall velocities are increased. Increasing snow bulk density reduces its collection cross-section. Increasing terminal fall velocities of large particles removes them quickly from the upper levels in stratiform region. Variations of snow aggregates' density and terminal fall velocity with their sizes in the original scheme are plotted in Figure 8 in solid lines. In experiment 'rho_vt', the minimum density for aggregates is set at 0.2 g cm^{-3}, in contrast to 0.03 g cm^{-3} in the original scheme (dashed line in Figure 8). This is more than doubling of aggregates' bulk density for particles larger than about 0.6 mm. In the meantime, all particles' terminal fall velocities are doubled, as also shown in Figure 8. The simulated radar reflectivity and 85 GHz BT statistics are shown in Figure 9(a) (C-band radar reflectivity CFADs), 9(b) (PR reflectivity CFADs), and 9(c) (TMI 85 GHz PCT distributions). Comparing the first row of Figure 9 with plots in Figure 5, one finds that although experiment 'rho_vt' reduces radar reflectivity in the stratiform region by several dB, it is still considerably higher than observations, especially above the melting level. The slopes of the increasing radar reflectivity with decreasing heights are similarly curved as in the control run, in contrast to the observed linear slope in both surface and TRMM radar.

4.2.2. *Temperature dependency of E_c*

Another set of sensitivity simulations are carried out on $E_c(T)$. Experiment 'Ec' represents our best match among many trials. $E_c(T)$ used in this simulation is plotted as the solid line in Figure 7. When warmer than -6°C, the revised $E_c(T)$ are in range with measurements. However, $E_c(T)$ have to be reduced drastically from their original values at lower temperatures in order for the stratiform region radar reflectivity to match observations. The middle row in Figure 9 is the simulated C-band (9(d)) and PR (9(e)) reflectivity CFADs, and 85 GHz PCT distributions (9(f)). Compared with the original simulations shown in Figure 5(d) and (e), experiment 'Ec' improved all qualitative features in radar CFADs comparisons. For example, radar reflectivity increases linearly with decreasing height above the melting band for both radar frequencies. Radar reflectivity profiles have also substantially lower values, with the mean dBZ now in line with observations.

4.2.3. *Break-up of large snow aggregates*

Experiment 'sbreakup' is one of our tests to add a sink term to the snow aggregate growth equation in order to reduce the simulated snow aggregate size. Break-ups of large pristine snow crystals have been widely observed, but there are no quantitative measurements of how large snow aggregates would break up, either spontaneously or through collisions. In this experiment, a simple binary break-up procedure is added to the original bin microphysical scheme. A constant probability is assigned to the largest of the particles, with its value decreasing with decreasing particle sizes, down to zero at a certain size. Each break-up event results in two smaller particles of equal mass. The last row in Figure 9 shows results from experiment 'sbreakup'. In this simulation, the probability of aggregates' break-up decreases linearly from 0.8 for particles with melted radius of 3 mm down to 0 for particles with melted radius of 0.5 mm. There is no break-up for particles smaller than 0.5 mm.

Figure 9(g) and (h) show that adding a simple break-up scheme lowers radar reflectivity values, both at the surface and above the melting level. The maximum radar reflectivity above the melting level is less than 30 dBZ for both C-band and PR radar, consistent with observations shown in Figure 5(a) and (b). However, experiment 'sbreakup' cannot reproduce the linear slope of radar CFADs shown in both observations and experiment 'Ec'. The high growth rate above 7 km results in a fast increase of radar reflectivity along the particles' falling paths. Only after aggregates become large enough does the break-up process kick in and keep the radar reflectivity value below 30 dBZ.

4.3. *New discrepancy in 85 GHz BT and its diagnosis*

All three sensitivity experiments described in the previous subsection more or less reduced mean snow aggregate size, and therefore radar reflectivity in the stratiform region, as shown in Figure 9. However, all of them have produced decidedly worse comparisons in 85 GHz PCT distributions. The distributions simulated in the control run (Figure 5(f)) compare well with TRMM statistics (Figure 5(c)). In the sensitivity simulations, however, the distinct jump around 220 K in the control experiment is completely missing (Figure 9(c), (f) and (i)). PCT distributions in Figure 9 increase rather smoothly to a weak peak at around 180 K. The mean BT is also reduced from 213 K in the control run down to 197–200 K, further away from the observed 224 K mean. This is a common problem in 'tuning' a microphysical scheme according to a single set of observations; one fixes one thing by breaking another. It also shows the intricate relationships between different microphysical processes and their interactions with dynamics. In this section, we try to isolate the reasons for these discrepancies and search for a possible solution.

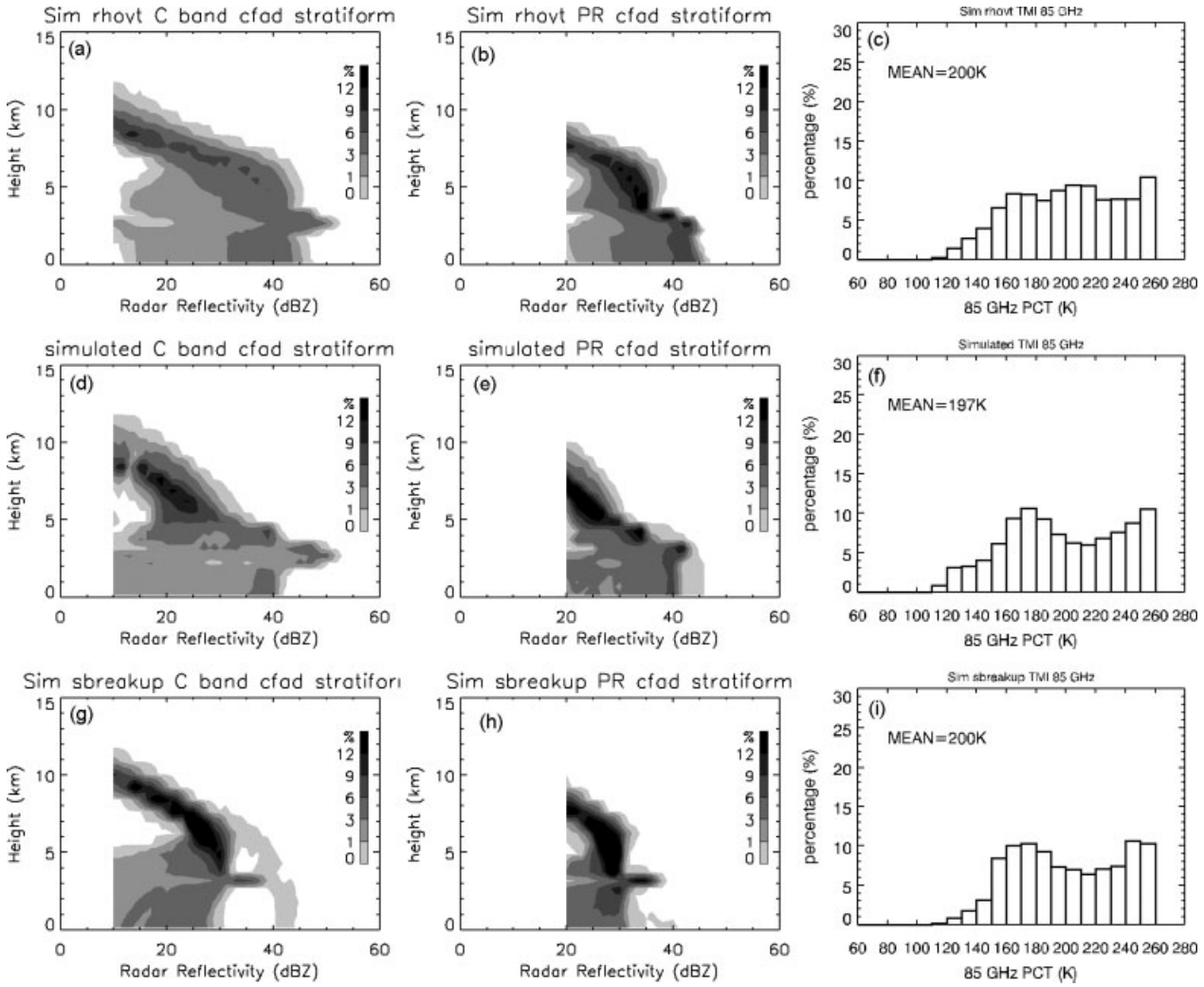

Figure 9. Simulated results from three sensitivity simulations. (a) C-band radar CFADs for experiment 'rho_vt'; (b) TRMM PR CFADs for experiment 'rho_vt'; (c) TMI 85 GHz PCT probability density distributions for experiment 'rho_vt'; (d) C-band radar CFADs for experiment 'Ec'; (e) TRMM PR CFADs for experiment 'Ec'; (f) TMI 85 GHz PCT probability density distributions for experiment 'Ec'; (g) C-band radar CFADs for experiment 'sbreakup'; (h) TRMM PR CFADs for experiment 'sbreakup'; (i) TMI 85 GHz PCT probability density distributions for experiment 'sbreakup'.

Unlike radar reflectivity at mid-level stratiform regions, where snow aggregates dominate the signal, a microwave radiometer observes column integrations of emission and scattering of radiances by all hydrometeor species, in both water- and ice-phase. Different species contribute to the BT signal in different ways depending on their phases, sizes, shapes, densities and associated electromagnetic properties. At 85 GHz over land, TMI observes BT depression over a warm surface background. A higher amount of ice content in a column generally means lower BT. When BT is calculated for individual species, their contributions are more or less comparable. Therefore, we focus our analyses on finding the species that has the largest change in favour of lowering 85 GHz BT in experiment 'Ec', which turns out to be graupel. Figure 10 is an example of instantaneous number concentration and mass content of graupel in the control run and experiment 'Ec', at $t = 12$ hours. After adjusting $E_c(T)$, graupel remains at slightly lower heights and its total amount decreases. However, the most dramatic change comes in its number concentrations. In the convective core, graupel number concentration decreases from more than 100 L^{-1} in the control run down to about 30 L^{-1} in experiment 'Ec'. In the stratiform region, it decreases from about 20 L^{-1} to about 10 L^{-1}. The resulting 20–30% increase in the mean graupel size is the main reason for the decrease of mean 85 GHz PCT, as well as the shifting of its distribution. In addition, a large increase of ice crystals in both amount and size contributes to the BT depression (cf. Figure 11(a) and (b)), but to a lesser extent compared with graupel.

4.4. *Further improvements of microphysical scheme*

In order to improve the 85 GHz PCT comparisons, we need to understand the causes of increasing mean graupel size, after the mean sizes of snow aggregates are reduced. Figure 11 shows vertical profiles of various hydrometeor species averaged over the mature stage for three different simulations carried out in this study. Comparing Figure 11(a) and 11(b) one finds that by reducing $E_c(T)$ in experiment 'Ec', a large amount of ice content is shifted from snow aggregates to pristine crystals, especially between 5 and 10 km. This shift affects graupel formation in two ways: First, compared with large snow aggregates, small ice particles interact less efficiently with supercooled cloud droplets in the convective region to form graupel. As a result, fewer graupel are formed in the convective region. This leaves more supercooled water available for the Bergeron–Findeisen

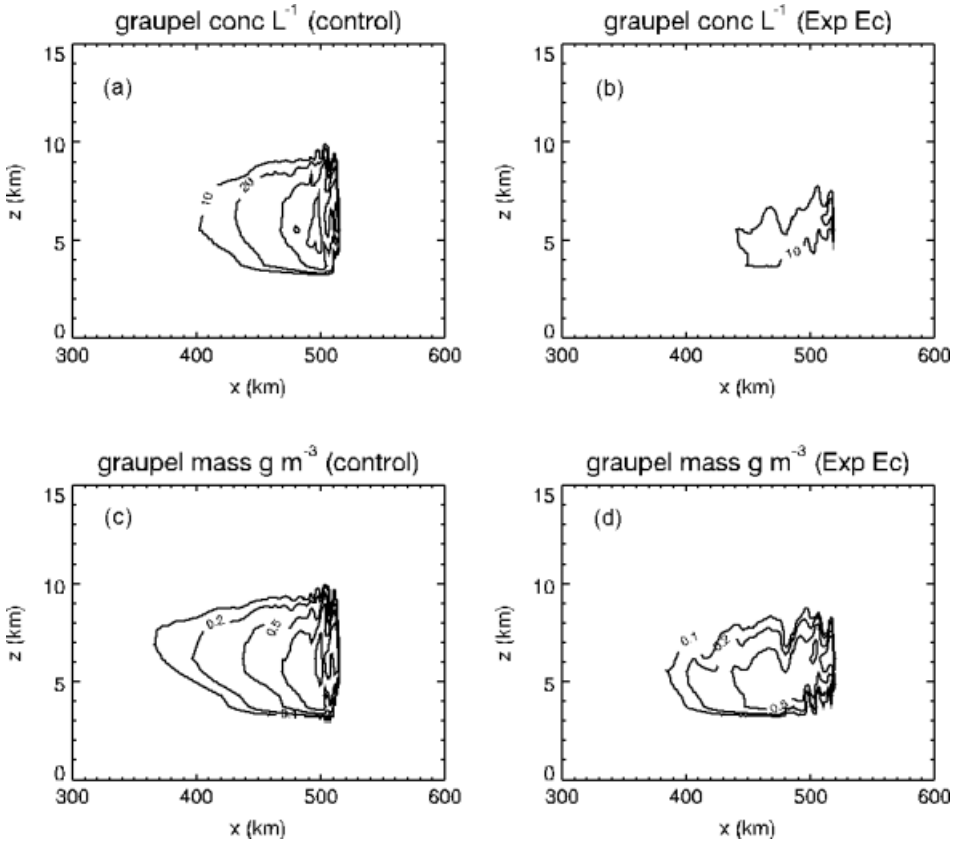

Figure 10. Instantaneous graupel number concentration in the control run (a) and experiment 'Ec' (b) at the end modelling time. The contour lines are 10, 20, 50, 100, 200 and 500 L^{-3}. Graupel mass contents at the same time are plotted in (c) for the control run and (d) for experiment 'Ec'. The contour lines are 0.1, 0.2, 0.5, 1, 2 and 5 g m^{-3}.

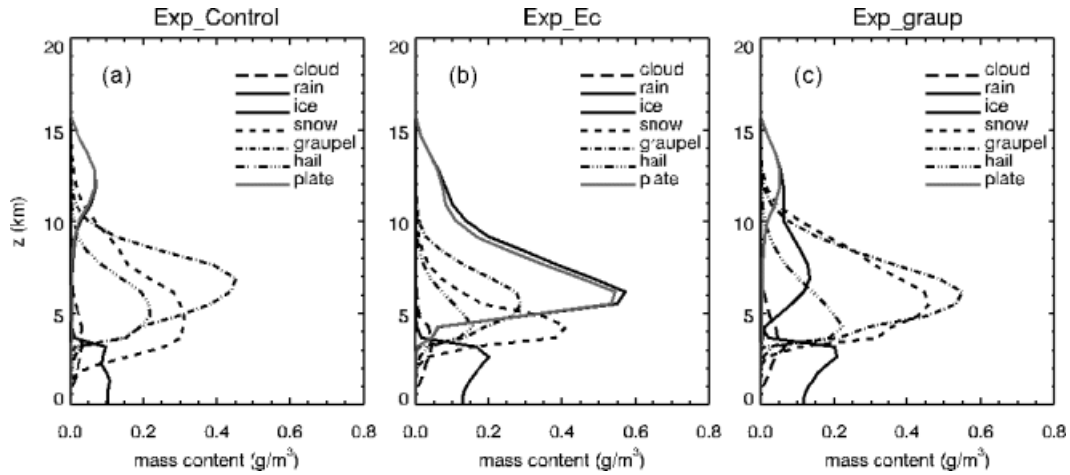

Figure 11. Mean vertical profiles of various hydrometeors during the mature stage of the simulated squall line for three experiments: (a) control run; (b) experiment 'Ec'; and (c) experiment 'graup'. Long dashed lines represent cloud water; solid lines represent rain water at lower heights and ice crystal at upper heights; short dashed lines represent snow aggregates; dash-dot lines represent graupel; dash-dot-dot-dot lines represent hail; and the grey solid line represent plate-shaped ice crystals which is the dominant type among the three different pristine ice species.

process (the depositional growth of ice-phase particles at the expenses of evaporation of water-phase particles). As a result, mean sizes of both graupel and pristine ice become larger in experiment 'Ec' compared with the control run (cf. Figure 10). This leads to the reduction of the 85 GHz BT. On the other hand, when the amount of snow aggregates is reduced, the only sink term for graupel, i.e. its collection by large snow aggregates to form snow particles, is reduced as well. Thus fewer graupel stays longer with the system without being removed in experiment 'Ec'. These relatively large graupel are detrained to the stratiform region, causing reduction and redistribution of 85 GHz BT as shown in Figure 9(c).

In this section, we attempt to modify the bin scheme to form more, smaller graupel while keeping the size of snow aggregates in check. Numerous sensitivity tests have been carried out to study the interactions between water- and ice-phase particles to form graupel. Again, there may be multiple solutions to this problem. Similar to discussions in section 4.2, we attempt to achieve the goal with the least amount of modification based on physics. Experiment 'graup' represents our best result under this philosophy.

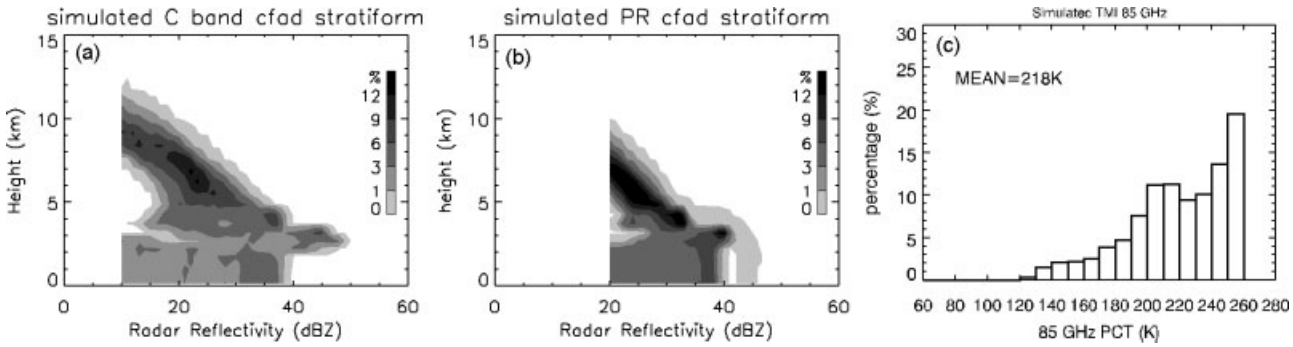

Figure 12. Same as Figure 9, except for experiment 'graup'.

In our bin microphysical scheme, one of the uncertainties in graupel formation comes from the subjective thresholds where the end product of coalescence of ice- and water-phase particles is assigned. For example, in the bin scheme, snow aggregates collecting cloud droplets may form either graupel or snow. When cloud liquid content is larger than 1 g m^{-3}, the end product is graupel. When cloud liquid content is less than 1 g m^{-3}, the end product can be either aggregates or graupel depending on its size. The threshold size is set at the 17th size bin (2.2×10^{-6} g) in the original scheme where particles smaller than that size remain as aggregates. As previously noted, these thresholds are empirically based and subjective. Two thresholds have been modified in experiment 'graup'. First, the size threshold separating aggregates from graupel as the end product of snow aggregates collecting cloud droplets is increased from the 17th to the 22nd size bin (7.0×10^{-5} g). This modification reduces formation of medium-size graupel which fall slowly enough to affect the 85 GHz BT in the stratiform region. Graupel larger than 7.0×10^{-5} g generally precipitate out quickly, thus have little impact on the stratiform BT. To increase graupel number concentration, similar modification is also applied to ice crystal collecting cloud droplets, in the direction of increasing small graupel concentrations. When ice crystals collect cloud droplets, smaller particles remain as crystals, while larger ones become graupel. In experiment 'graup', the threshold is lowered from the 17th to the 13th size bin (1.4×10^{-7}g) so that more, smaller graupel are generated. This dramatically reduces the total amount of ice crystals between 5 and 10 km, as shown in Figure 11(c). At the same time, there are more, smaller graupel in experiment 'graup' competing for the available water vapour, which further reduces mean graupel size. In experiment 'graup', both snow and graupel content increase compared with experiment 'Ec', at the expense of ice crystals. Meanwhile, both surface rainfall and squall-line structure remain similar for all three simulations as indicated in Figure 11. Note that in experiment 'graup', we are able to increase the temperature dependency of E_c compared with experiment 'Ec', as shown in the dash-dot-dot-dot line in Figure 7. Here E_c is fixed at 0.01 from -20 down to -40°C. Although they are still smaller than observations, this set of E_c represents a large increase from experiment 'Ec', which adjusts temperature dependency of E_c only.

Statistics for experiment 'graup' are shown in Figure 12, in the same format and scale as in Figures 5 and 9. Radar reflectivity CFADs in Figure 12(a) and (b) are very similar to their counterparts in Figure 9(a) and (b). There are slight reductions in radar reflectivity, about 1–2 dBZ, in experiment 'graup' compared with experiment 'Ec'. The major improvement comes in the probability density distribution in Figure 12(c). The unrealistic PCT peak between 170 and 180 K in Figure 9(c) is removed in experiment 'graup'. The majority of the data points are shifted back to above 200 K, more closely reflecting TRMM statistics. The mean PCT increased 21 K to 218 K, again a much better comparison with the observation. There are still discrepancies in details. For example, the abrupt increase of the distribution at around 220 K in Figure 5(c) is less prominent in Figure 12(c). However, given the many uncertainties in various aspects in the modelling other than microphysics, results in experiment 'graup' represent a major improvement in comparisons with long-term satellite statistics.

5. Summary and discussion

A squall line over the central southern USA (PRE-STORM, 10–11 June 1985) is simulated using the GCE model with a detailed spectral bin microphysical scheme. After comparisons with published, surface-based observations and retrievals (Li *et al.*, 2009), the model results are further compared with ground-based C-band radar as well as PR reflectivity and TMI 85 GHz BT from the TRMM satellite. This study is unique in two aspects: First, it uses long-term satellite observations of robust features in squall lines, especially in the stratiform region, whereas most model validations use the same case-study. Second, it evaluates and improves a bin spectral microphysical scheme which explicitly simulates particle size distributions. Instead of comparing direct model output with retrieved quantities from observations (i.e. surface rainfall, column water contents), a forward radiative transfer model (simulator) is used to calculate satellite-observed signals using the modelled particle size distributions. In this approach, if discrepancies occur, as they did, the reasons are readily linked to model physics.

It is first established that the stratiform region in squall lines in the central USA during late spring and early summer has very robust structures. Comparisons of radar reflectivity CFADs and distributions of 85 GHz PCT between all individual cases and composites over a 9-year period of TRMM observation show very consistent features. Surface C-band radar observations during the PRE-STORM experiment provide further corroboration. Comparisons between simulated radar CFADs and observations reveal that the model overestimates stratiform radar reflectivity by about 10 dBZ for both C-band radar and TRMM PR. Diagnostic study shows that simulated snow aggregates in the stratiform region are too large.

Three sets of independent sensitivity simulations are performed in this study to reduce simulated radar reflectivity in the stratiform region. Experiment 'rho_vt' increases both snow aggregates' density and their fall velocity; experiment 'Ec' reduces the temperature dependency of ice-phase particles' collection efficiencies, especially at low temperatures; experiment 'sbreakup' adds a binary break-up scheme for large aggregates as a sink term in the snow aggregates' growth equation. All these methods reduce simulated radar reflectivity. However, increasing the aggregates' density and fall velocity is not able to reduce radar reflectivity enough to match the observations. Adding the break-up process for large aggregates results in better comparisons with absolute values of radar reflectivity, but it fails to produce the observed linear slope in radar CFADs. Experiment 'Ec' has the best comparison with observations. However, this does not necessarily mean that experiment 'Ec' is the unique, or even a correct solution. It is quite possible that all three factors contribute to a possible solution. However, in a situation where there are many uncertainties with few constraints in the microphysics, our general guidance is to find the most important physical process while keeping the modifications and discussions as simple as possible.

Further study shows that while PR comparison becomes good in experiment 'Ec', the probability density distributions of the 85 GHz PCT, which agreed relatively well with the observation in the original scheme, are now distorted, due to decreased sizes of snow aggregates. The fewer but larger graupel simulated in experiment 'Ec' are responsible for the excessive 85 GHz PCT depression. Another sensitivity simulation, 'graup', further adjusts end products of ice crystals/snow aggregates collecting droplets in order to increase the number concentration and reduce the size of graupel. The improved simulations in experiment 'graup' compare reasonably well with both PR and TMI observations.

Several notes need to be made on modifications of $E_c(T)$ and graupel formation parameters in our sensitivity studies:

First, the $E_c(T)$ profile used in experiment 'Ec' is relatively low and does not consider some well-observed phenomena such as the increase of E_c at around -15°C. This is kept for its simplicity and is fine in this particular case because the overwhelming majority of pristine ice crystals simulated in this case are of the plate type (cf. Figure 11(a)), whose collection efficiencies may be low at cold temperatures. This result should not be extrapolated to other systems such as synoptic snow events where dendrites are abundant. Furthermore, collection coefficient is only one of the many uncertainties in calculating the collection kernel. Density, terminal fall velocity, shape and orientation of ice-phase particles all contribute to variations of the collection kernel. Future research is needed in order to separate and quantify these different mechanisms. Meanwhile, two examples of actual values of collection kernels K_{ij} used in experiment 'graup' are given in the appendix for reference.

Second, the 2D framework used in this study may exacerbate the overestimation of aggregate sizes, too. Cotton *et al.* (1995) suggested that the mid-level air in front of a squall system also contributes to the stratiform region, especially near the transition zone. This air mass flows around the leading convective cores. It may not bring as many ice-phase particles as the air detrained directly from the leading convection. In a 2D framework, this cross-line flow cannot be properly simulated. Our future 3D case-studies will address these issues.

Third, in the paradigm of dry aggregates–graupel–hail separation, there are inevitable assumptions that separate different species, as we have shown in experiment 'graup'. We are in the process of including an additional variable, the rimed fraction in snow aggregates, in order to separate dry aggregates and graupel more objectively. However, current discussions remain useful for many of the simple microphysical schemes that do not consider rimed fraction explicitly.

Our study shows that multi-sensor, long-term TRMM observations can provide very useful constraints, and lead to significant improvements in model microphysics. The spectral bin microphysical scheme used in this study also allows for direct modifications of microphysical processes, in contrast to bulk microphysical schemes where the assumed particle size distributions are almost always the first to be questioned. However, the complex microphysical processes always have many more degrees of freedom than useful constraints provided by observations. The improvements presented in this paper are only one possible solution. One can hope that using more independent observations and *in situ* measurements will reduce some of the uncertainties discussed in this study. For example, both TRMM satellite and surface C-band radar are designed for precipitation measurements. They are not sensitive to the many smaller, non-precipitating particles which are important constituents of cloud systems and contribute significantly to global radiation budget through, for example, formation of anvil clouds. Our future study will include cloud radar, both surface-based and space-borne, and/or higher-frequency passive microwave sensors (e.g. 183 GHz) to further constrain small ice-phase particles simulated in the cloud model. In addition, *in situ* measurements will also be used to validate the simulated particle size distributions. Only through combinations of laboratory experiments, *in situ* measurements, remote sensing, as well as numerical modelling at various scales can we advance our understanding and representation of microphysics in clouds and cloud systems.

Acknowledgements

The authors wish to thank A.P. Khain at the Hebrew University of Jerusalem and an anonymous reviewer for their constructive and detailed suggestions that led to substantial improvements in this manuscript. We also thank R.C. Srivastava at the University of Chicago for his careful editing. Lin Tian, Bob Meneghini, and Bill Olson at NASA/GSFC have offered many of their insights on radar and microwave radiation observations and theories. This research is mainly supported by NASA headquarters and the NASA TRMM Mission. The authors are grateful to R. Kadar at NASA headquarters for his support in this research. Acknowledgement is also made to NASA GSFC for computer time used in this research.

Appendix.

Collection Kernel K_{Ij} Used in Sensitivity Test 'Graup'

Table AI is for snow aggregates collecting plate crystals. Table AII is for snow aggregates collecting themselves. The unit is $\mathrm{cm}^{-3}\mathrm{g}^{-1}\mathrm{s}^{-1}$. All values are at $T = -10^\circ$C.

Table AI. Collection kernel K_{ij} for snow aggregates collecting plates, in the unit of $cm^{-3}g^{-1}s^{-1}$, at $-10°C$, in sensitivity test 'graup'.

Mass(g)	3.4 $\times10^{-11}$	1.3 $\times10^{-10}$	5.4 $\times10^{-10}$	2.1 $\times10^{-9}$	8.6 $\times10^{-9}$	3.4 $\times10^{-8}$	1.4 $\times10^{-7}$	5.5 $\times10^{-7}$	2.2 $\times10^{-6}$	8.8 $\times10^{-6}$	3.5 $\times10^{-5}$	1.4 $\times10^{-4}$	5.6 $\times10^{-4}$	2.2 $\times10^{-3}$	9.0 $\times10^{-3}$	3.6 $\times10^{-2}$
3.4 $\times10^{-11}$	.000	.000	.000	.000	.000	.000	.000	.000	.000	.001	.003	.008	.016	.030	.055	.105
1.3 $\times10^{-10}$	.000	.000	.000	.000	.000	.000	.000	.000	.001	.002	.005	.012	.025	.046	.084	.157
5.4 $\times10^{-10}$	.000	.000	.000	.000	.000	.000	.000	.000	.001	.003	.008	.019	.039	.072	.131	.239
2.1 $\times10^{-9}$	.000	.000	.000	.000	.000	.000	.000	.000	.001	.005	.013	.030	.063	.115	.205	.371
8.6 $\times10^{-9}$	.000	.000	.000	.000	.000	.000	.000	.000	.002	.008	.020	.049	.100	.182	.324	.581
3.4 $\times10^{-8}$	.000	.000	.000	.000	.000	.000	.000	.000	.002	.009	.033	.078	.160	.289	.511	.910
1.4 $\times10^{-7}$	.000	.000	.000	.000	.000	.000	.000	.000	.002	.009	.039	.124	.252	.452	.796	1.41
5.5 $\times10^{-7}$	.000	.000	.000	.000	.000	.000	.000	.000	.001	.008	.036	.150	.388	.690	1.21	2.13
2.2 $\times10^{-6}$	.000	.000	.000	.001	.001	.001	.001	.004	.000	.005	.030	.136	.476	1.05	1.81	3.18
8.8 $\times10^{-6}$	.001	.001	.002	.003	.004	.004	.005	.006	.014	.001	.019	.111	.408	1.20	2.56	4.45
3.5 $\times10^{-5}$	.002	.003	.006	.010	.016	.017	.019	.021	.021	.019	.004	.073	.309	.906	2.57	5.65
1.4 $\times10^{-4}$	.005	.007	.013	.023	.040	.065	.070	.075	.074	.074	.064	.000	.169	.510	1.44	4.19
.56 $\times10^{-4}$	.010	.017	.029	.051	.089	.158	.261	.273	.264	.256	.243	.018	.082	.044	.000	0.28
2.2 $\times10^{-3}$	.022	.035	.060	.105	.183	.329	.566	.945	.907	.849	.780	.644	.573	.847	1.65	3.61
9.0 $\times10^{-3}$	.050	.077	.131	.227	.392	.687	1.20	2.06	3.32	3.13	2.87	2.48	2.45	3.43	5.97	12.0
3.6 $\times10^{-2}$	.104	.158	.266	.455	.781	1.36	2.35	4.01	6.48	10.3	9.60	8.18	7.71	9.57	14.3	24.7

Table AII. Collection kernel K_{ij} for snow aggregates collecting themselves, in the unit of $cm^{-3}g^{-1}s^{-1}$, at $-10°C$, in sensitivity test 'graup'.

Mass(g)	3.4 $\times10^{-11}$	1.3 $\times10^{-10}$	5.4 $\times10^{-10}$	2.1 $\times10^{-9}$	8.6 $\times10^{-9}$	3.4 $\times10^{-8}$	1.4 $\times10^{-7}$	5.5 $\times10^{-7}$	2.2 $\times10^{-6}$	8.8 $\times10^{-6}$	3.5 $\times10^{-5}$	1.4 $\times10^{-4}$	5.6 $\times10^{-4}$	2.2 $\times10^{-3}$	9.0 $\times10^{-3}$	3.6 $\times10^{-2}$
3.4 $\times10^{-11}$	.000	.000	.000	.000	.000	.000	.000	.000	.000	.000	.001	.002	.004	.009	.020	.042
1.3 $\times10^{-10}$	.000	.000	.000	.000	.000	.000	.000	.000	.000	.000	.001	.003	.007	.014	.031	.063
5.4 $\times10^{-10}$	.000	.000	.000	.000	.000	.000	.000	.000	.000	.001	.002	.005	.011	.022	.048	.098
2.1 $\times10^{-9}$	.000	.000	.000	.000	.000	.000	.000	.000	.000	.001	.003	.008	.017	.035	.076	.153
8.6 $\times10^{-9}$	.000	.000	.000	.000	.000	.000	.000	.000	.000	.001	.005	.012	.027	.056	.121	.241
3.4 $\times10^{-8}$	.000	.000	.000	.000	.000	.000	.000	.000	.000	.001	.006	.020	.044	.090	.192	.381
1.4 $\times10^{-7}$	.000	.000	.000	.000	.000	.000	.000	.000	.000	.002	.007	.025	.070	.142	.303	.600
5.5 $\times10^{-7}$	.000	.000	.000	.000	.000	.000	.000	.000	.000	.002	.006	.025	.095	.221	.473	.934
2.2 $\times10^{-6}$	.000	.000	.000	.000	.000	.000	.000	.000	.000	.001	.006	.023	.091	.322	.752	1.48
8.8 $\times10^{-6}$	.000	.000	.001	.001	.001	.001	.002	.002	.001	.000	.004	.020	.081	.292	1.12	2.31
3.5 $\times10^{-5}$	.001	.001	.002	.003	.005	.006	.007	.006	.006	.004	.000	.015	.069	.249	.993	3.44
1.4 $\times10^{-4}$	.002	.003	.005	.008	.012	.020	.025	.025	.023	.020	.015	.000	.048	.197	.837	2.94
5.6 $\times10^{-4}$	.004	.007	.011	.017	.027	.044	.070	.095	.091	.081	.069	.048	.000	.119	.672	2.39
2.2 $\times10^{-3}$	.009	.014	.022	.035	.056	.090	.142	.221	.322	.292	.249	.197	.119	.000	.558	2.07
9.0 $\times10^{-3}$	.020	.031	.048	.076	.121	.192	.303	.473	.752	1.12	.993	.837	.672	.558	.000	1.09
3.6 $\times10^{-2}$	.042	.063	.098	.153	.241	.381	.600	.934	1.48	2.31	3.44	2.94	2.39	2.07	1.09	.000

References

Biggerstaff MI, Houze Jr RA. 1993. Kinematics and microphysics of the transition zone of the 10–11 June 1985 squall line. *J. Atmos. Sci.* **50**: 3091–3110.

Böhm HP. 1989. A general equation for the terminal fall speed of solid hydrometeors. *J. Atmos. Sci.* **46**: 2419–2427.

Bohren CF, Battan LJ. 1980. Radar backscattering by inhomogeneous precipitation particles. *J. Atmos. Sci.* **37**: 1821–1827.

Brandes EA, Ikeda K, Zhang G, Sch&onhuber M, Rasmussen RM. 2007. A statistical and physical description of hydrometeor distributions in Colorado snowstorms using a video disdrometer. *J. Appl. Meteorol. Clim.* **46**: 634–650.

Brandes EA, Ikeda K, Thompson G, Sch&onhuber M. 2008. Aggregate terminal velocity/temperature relations. *J. Appl. Meteorol. Clim.* **47**: 2729–2736.

Braun SA, Houze Jr RA. 1996. The heat budget of a midlatitude squall line and implications for potential vorticity production. *J. Atmos. Sci.* **53**: 1217–1240.

Carrio GG, Nicolini M. 2002. An alternative procedure to evaluate number concentration rates in two-moment bulk microphysical schemes. *Atmos. Res.* **65**: 93–108.

Chen J-P, Liu S-T. 2004. Physically based two-moment bulkwater parametrization for warm-cloud microphysics. *Q. J. R. Meteorol. Soc.* **130**: 51–78.

Clark TL. 1973. Numerical modeling of the dynamics and microphysics of warm cumulus convection. *J. Atmos. Sci.* **30**: 857–878.

Cotton WR, Stephens MA, Nehrkorn T, Tripoli GJ. 1982. The Colorado State University three-dimensional cloud/mesoscale model – 1982. Part II: Ice phase parameterization. *J. Rech. Atmos.* **16**: 295–320.

Cotton WR, Tripoli GJ, Rauber RM, Mulvihill EA. 1986. Numerical simulation of the effects of varying ice crystal nucleation rates and aggregation processes on orographic snowfall. *J. Clim. Appl. Meteorol.* **25**: 1658–1680.

Cotton WR, Alexander GD, Hertenstein R, Walko RL, McAnelly RL, Nicholls M. 1995. Cloud venting: A review and some new global annual estimates. *Earth Sci. Rev.* **39**: 169–206.

Dudhia J, Moncrieff MW. 1989. A three-dimensional numerical study of an Oklahoma squall line containing right-flank supercells. *J. Atmos. Sci.* **46**: 3363–3391.

Feingold G, Stevens B, Cotton WR, Walko RL. 1994. An explicit cloud microphysics/LES model designed to simulate the Twomey effect. *Atmos. Res.* **33**: 207–233.

Ferrier BS. 1994. A double-moment multiple-phase four-class bulk ice scheme. Part I: Description. *J. Atmos. Sci.* **51**: 249–280.

Field PR, Heymsfield AJ. 2003. Aggregation and scaling of ice crystal size distributions. *J. Atmos. Sci.* **60**: 544–560.

Field PR, Heymsfield AJ, Bansemer A. 2006. A test of ice self-collection kernels using aircraft data. *J. Atmos. Sci.* **63**: 651–666.

Fovell RG, Dailey PS. 1995. The temporal behavior of numerically simulated multicell-type storms. Part I: Modes of behavior. *J. Atmos. Sci.* **52**: 2073–2095.

Fujita TT. 1981. Tornadoes and downbursts in the context of generalized planetary scales. *J. Atmos. Sci.* **38**: 1511–1534.

Gallus Jr WA, Johnson RH. 1991. Heat and moisture budgets of an intense midlatitude squall line. *J. Atmos. Sci.* **48**: 122–146.

Geresdi I. 1998. Idealized simulation of the Colorado hailstorm case: Comparison of bulk and detailed microphysics. *Atmos. Res.* **45**: 237–252.

Grabowski WW, Wu X, Moncrieff MW. 1999. Cloud resolving modeling of tropical cloud systems during phase III of GATE. Part III: Effects of cloud microphysics. *J. Atmos. Sci.* **56**: 2384–2402.

Hall WD. 1980. A detailed microphysical model within a two-dimensional dynamic framework: Model description and preliminary results. *J. Atmos. Sci.* **37**: 2486–2507.

Hallgren RE, Hosler CL. 1960. Preliminary results on the aggregation of ice crystals. Pp 257–263 in *Physics of precipitation,* Weickmann H (ed). Geophys. Monogr. Am. Geophys. Union No. 5.

Hashino T, Tripoli GJ. 2007. The Spectral Ice Habit Prediction System (SHIPS). Part I: Model description and simulation of the vapor deposition process. *J. Atmos. Sci.* **64**: 2210–2237.

Heymsfield AJ. 2003. Properties of tropical and midlatitude ice cloud particle ensembles. Part I: Median mass diameters and terminal velocities. *J. Atmos. Sci.* **60**: 2573–2591.

Hosler CL, Jensen DC, Goldshlak L. 1957. On the aggregation of ice crystals to form snow. *J. Meteorol.* **14**: 415–420.

Houze Jr RA. 1989. Observed structure of mesoscale convective systems and implications for large-scale heating. *Q. J. R. Meteorol. Soc.* **115**: 425–461.

Houze Jr RA, Smull BF, Dodge P. 1990. Mesoscale organization of springtime rainstorms in Oklahoma. *Mon. Weather Rev.* **118**: 613–654.

Johnson RH, Hamilton PJ. 1988. The relationship of surface pressure features to the precipitation and airflow structure of an intense midlatitude squall line. *Mon. Weather Rev.* **116**: 1444–1472.

Kajikawa M, Heymsfield AJ. 1989. Aggregation of ice crystals in cirrus. *J. Atmos. Sci.* **46**: 3108–3121.

Karbou F. 2008. http://www.cnrm.meteo.fr/gmap/mwemis/cal_emis.html.

Kessler E. 1969. On the distribution and continuity of water substance in atmospheric circulation. *Meteorol. Monogr., American Meteorological Society* **32**: 1065–1092.

Khain AP, Sednev I. 1996. Simulation of precipitation formation in the eastern Mediterranean coastal zone using a spectral microphysics cloud ensemble model. *Atmos. Res.* **43**: 77–110.

Khain AP, Ovtchinnikov M, Pinsky M, Pokrovsky A, Krugliak H. 2000. Notes on the state-of-the-art numerical modeling of cloud microphysics. *Atmos. Res.* **55**: 159–224.

Khain AP, Pokrovsky A, Pinsky M, Seifert A, Phillips V. 2004. Simulation of effects of atmospheric aerosols on deep turbulent convective clouds using a spectral microphysics mixed-phase cumulus cloud model. Part I: Model description and possible applications. *J. Atmos. Sci.* **61**: 2963–2982.

Krueger SK, Fu Q, Liou KN, Chin H-NS. 1995. Improvements of an ice-phase microphysics parameterization for use in numerical simulations of tropical convection. *J. Appl. Meteorol.* **34**: 281–287.

Kummerow C. 1993. On the accuracy of the Eddington approximation for radiative transfer in the microwave frequencies. *J. Geophys. Res.* **98**: 2757–2765.

Lang S, Tao W-K, Cifelli R, Olson WS, Halverson J, Rutledge S, Simpson J. 2007. Improving simulations of convective systems from TRMM LBA: Easterly and westerly regimes. *J. Atmos. Sci.* **64**: 1141–1164.

Li X, Tao W-K, Khain AP, Simpson J, Johnson DE. 2009. Sensitivity of a cloud-resolving model to bulk and explicit bin microphysical schemes. Part I: Comparisons. *J. Atmos. Sci.* **66**: 3–21.

Li Y, Zipser EJ, Krueger SK, Zulauf MA. 2008. Cloud-resolving modeling of deep convection during KWAJEX. Part I: Comparison to TRMM satellite and ground-based radar observations. *Mon. Weather Rev.* **136**: 2699–2712.

Lin Y-L, Farley RD, Orville HD. 1983. Bulk parameterization of the snow field in a cloud model. *J. Clim. Appl. Meteorol.* **22**: 1065–1092.

Liu C, Zipser EJ, Cecil DJ, Nesbitt SW, Sherwood S. 2008. A cloud and precipitation feature database from nine years of TRMM observations. *J. Appl. Meteorol. Clim.* **47**: 2712–2728.

Locatelli JD, Hobbs PV. 1974. Fall speeds and masses of solid precipitation particles. *J. Geophys. Res.* **79**: 2185–2197.

Luo Y, Krueger SK, Mace GG, Xu K-M. 2003. Cirrus cloud properties from a cloud-resolving model simulation compared to cloud radar observations. *J. Atmos. Sci.* **60**: 510–525.

Luo Y, Xu K-M, Morrison H, McFarquhar G. 2008. Arctic mixed-phase clouds simulated by a cloud-resolving model: Comparison with ARM observations and sensitivity to microphysics parameterizations. *J. Atmos. Sci.* **65**: 1285–1303.

McCumber M, Tao W-K, Simpson J, Penc R, Soong S-T. 1991. Comparison of ice-phase microphysical parameterization schemes using numerical simulations of tropical convection. *J. Appl. Meteorol.* **30**: 985–1004.

Masunaga H, Kummerow CD. 2005. Combined radar and radiometer analysis of precipitation profiles for a parametric retrieval algorithm. *J. Atmos. Oceanic Technol.* **22**: 909–929.

Masunaga H, Satoh M, Miura H. 2008. A joint satellite and global cloud-resolving model analysis of a Madden–Julian Oscillation event: Model diagnosis. *J. Geophys. Res.* **113**: D17210, DOI:10.1029/2008JD009986.

Matsui T, Zeng X, Tao W-K, Masunaga H, Olson WS, Lang S. 2009. Evaluation of long-term cloud-resolving model simulations using satellite radiance observations and multifrequency satellite simulators. *J. Atmos. Oceanic Technol.* **26**: 1261–1274.

Meyers MP, DeMott PJ, Cotton WR. 1992. New primary ice-nucleation parameterizations in an explicit cloud model. *J. Appl. Meteorol.* **31**: 708–721.

Meyers MP, Walko RL, Harrington JY, Cotton WR. 1997. New RAMS cloud microphysics parameterization. Part II: The two-moment scheme. *Atmos. Res.* **45**: 3–39.

Milbrandt JA, Yau MK. 2005. A multimoment bulk microphysics parameterization. Part I: Analysis of the role of the spectral shape parameter. *J. Atmos. Sci.* **62**: 3051–3064.

Mitchell DL. 1988. Evolution of snow-size spectra in cyclonic storms. Part I: Snow growth by vapor deposition and aggregation. *J. Atmos. Sci.* **45**: 3431–3451.

Mitchell DL. 1994. A model predicting the evolution of ice particle size spectra and radiative properties of cirrus clouds. Part I: Microphysics. *J. Atmos. Sci.* **51**: 797–816.

Mitchell DL, Heymsfield AJ. 2005. Refinements in the treatment of ice particle terminal velocities, highlighting aggregates. *J. Atmos. Sci.* **62**: 1637–1644.
Morrison H, Pinto JO. 2005. Mesoscale modeling of springtime Arctic mixed-phase stratiform clouds using a new two-moment bulk microphysics scheme. *J. Atmos. Sci.* **62**: 3683–3704.
Murakami M. 1990. Numerical modeling of dynamical and microphysical evolution of an isolated convective cloud: The 19 July 1981 CCOPE cloud. *J. Meteorol. Soc. Jpn* **68**: 107–128.
Nesbitt SW, Zipser EJ, Cecil DJ. 2000. A census of precipitation features in the Tropics using TRMM: Radar, ice scattering, and lightning observations. *J. Climate* **13**: 4087–4106.
Ohtake T. 1970. Factors affecting the size distribution of raindrops and snowflakes. *J. Atmos. Sci.* **27**: 804–813.
Olson WS, Kummerow CD. 1996. Simulated retrieval of precipitation profiles from TRMM Microwave Imager and precipitation radar data. Pp 248–251 in *Preprints, Eighth Conference on satellite meteorology and oceanography, Atlanta, Georgia, USA*. American Meteorological Society.
Ovtchinnikov M, Kogan YL. 2000. An investigation of ice production mechanisms in small cumuliform clouds using a 3D model with explicit microphysics. Part II: Case study of New Mexico cumulus clouds. *J. Atmos. Sci.* **57**: 3004–3020.
Parker MD, Johnson RH. 2004. Simulated convective lines with leading precipitation. Part I: Governing dynamics. *J. Atmos. Sci.* **61**: 1637–1655.
Passarelli Jr RE. 1978. Theoretical and observational study of snow-size spectra and snowflake aggregation efficiencies. *J. Atmos. Sci.* **35**: 882–889.
Pruppacher HR, Klett JD. 1997. *Microphysics of clouds and precipitation.* Reidel: Dordrecht.
Reisin T, Levin Z, Tzivion S. 1996. Rain production in convective clouds as simulated in an axisymmetric model with detailed microphysics. Part I: Description of the model. *J. Atmos. Sci.* **53**: 497–519.
Reisner J, Rasmussen RM, Bruintjes RT. 1998. Explicit forecasting of supercooled liquid water in winter storms using the MM5 mesoscale model. *Q. J. R. Meteorol. Soc.* **124**: 1071–1107.
Rutledge SA, Hobbs PV. 1984. The mesoscale and microscale structure and organization of clouds and precipitation in midlatitude cyclones. XII: A diagnostic modeling study of precipitation development in narrow cold-front rainbands. *J. Atmos. Sci.* **41**: 2949–2972.
Rutledge SA, Houze Jr RA, Biggerstaff MI, Matejka T. 1988. The Oklahoma–Kansas mesoscale convective system of 10–11 June 1985: Precipitation structure and single-Doppler radar analysis. *Mon. Weather Rev.* **116**: 1409–1430.
Seifert A, Beheng KD. 2006. A two-moment cloud microphysics parameterization for mixed-phase clouds. Part 1: Model description. *Meteorol. Atmos. Phys.* **92**: 45–66.
Soong S-T. 1974. Numerical simulation of warm rain development in an axisymmetric cloud model. *J. Atmos. Sci.* **31**: 1262–1285.
Spencer RW, Goodman HM, Hood RE. 1989. Precipitation retrieval over land and ocean with the SSM/I: Identification and characteristics of the scattering signal. *J. Atmos. Oceanic Technol.* **6**: 254–273.
Srivastava RC. 1967. A study of the effect of precipitation on cumulus dynamics. *J. Atmos. Sci.* **24**: 36–45.
Stoelinga MT, Hobbs PV, Mass CF, Locatelli JD, Colle BA, Houze Jr RA, Rangno AL, Bond NA, Smull BF, Rasmussen RM, Thompson G, Colman BR. 2003. Improvement of microphysical parameterization through observational verification experiment. *Bull. Am. Meteorol. Soc.* **84**: 1807–1826.
Straka JM, Mansell ER. 2005. A bulk microphysics parameterization with multiple ice precipitation categories. *J. Appl. Meteorol.* **44**: 445–466.
Takahashi T. 1975. Tropical showers in an axisymmetric cloud model. *J. Atmos. Sci.* **32**: 1318–1330.
Tao W-K, Simpson J. 1989. Modeling study of a tropical squall-type convective line. *J. Atmos. Sci.* **46**: 177–202.
Tao W-K, Simpson J. 1993. Goddard Cumulus Ensemble model. Part I: Model description. *Terr. Atmos. Oceanic Sci.* **4**: 35–72.
Tao W-K, Simpson J, Soong S-T. 1991. Numerical simulation of a subtropical squall line over the Taiwan Strait. *Mon. Weather Rev.* **119**: 2699–2723.
Tao W-K, Simpson J, Sui C-H, Ferrier B, Lang S, Scala J, Chou M-D, Pickering K. 1993. Heating, moisture, and water budgets of tropical and midlatitude squall lines: Comparisons and sensitivity to longwave radiation. *J. Atmos. Sci.* **50**: 673–690.
Tao W-K, Scala JR, Ferrier B, Simpson J. 1995. The effect of melting processes on the development of a tropical and a midlatitude squall line. *J. Atmos. Sci.* **52**: 1934–1948.
Tao W-K, Lang S, Simpson J, Sui C-H, Ferrier B, Chou M-D. 1996. Mechanisms of cloud–radiation interaction in the Tropics and midlatitudes. *J. Atmos. Sci.* **53**: 2624–2651.
Tao W-K, Simpson J, Baker D, Braun S, Chou M-D, Ferrier B, Johnson D, Khain A, Lang S, Lynn B, Shie C-L, Starr D, Sui C-H, Wang Y, Wetzel P. 2003. Microphysics, radiation and surface processes in the Goddard Cumulus Ensemble (GCE) model. *Meteorol. Atmos. Phys.* **82**: 97–137.
Thompson G, Rasmussen RM, Manning K. 2004. Explicit forecasts of winter precipitation using an improved bulk microphysics scheme. Part I: Description and sensitivity analysis. *Mon. Weather Rev.* **132**: 519–542.
Thompson G, Field PR, Rasmussen RM, Hall WD. 2008. Explicit forecasts of winter precipitation using an improved bulk microphysics scheme. Part II: Implementation of a new snow parameterization. *Mon. Weather Rev.* **136**: 5095–5115.
Trier SB, Skamarock WC, LeMone MA, Parsons DB, Jorgensen DP. 1996. Structure and evolution of the 22 February 1993 TOGA COARE squall line: Numerical simulations. *J. Atmos. Sci.* **53**: 2861–2886.
Velasco I, Fritsch JM. 1987. Mesoscale convective complexes in the Americas. *J. Geophys. Res.* **92**: 9591–9613.
Wang C, Chang JS. 1993. A three-dimensional numerical model of cloud dynamics, microphysics, and chemistry. 1: Concepts and formulation. *J. Geophys. Res.* **98**: 14827–14844.
Weisman ML. 1993. The genesis of severe, long-lived bow echoes. *J. Atmos. Sci.* **50**: 645–670.
Weisman ML, Klemp JB, Rotunno R. 1988. Structure and evolution of numerically simulated squall lines. *J. Atmos. Sci.* **45**: 1990–2013.
Wiedner M, Prigent C, Pardo JR, Nuissier O, Chaboureau J-P, Pinty J-P, Mascart P. 2004. Modeling of passive microwave responses in convective situations using output from mesoscale models: Comparison with TRMM/TMI satellite observations. *J. Geophys. Res.* **109**: D06214, DOI:10.1029/2003JD004280.
Woods CP, Stoelinga MT, Locatelli JD. 2007. The IMPROVE-1 storm of 1–2 February 2001. Part III: Sensitivity of a mesoscale model simulation to the representation of snow particle types and testing of a bulk microphysical scheme with snow habit prediction. *J. Atmos. Sci.* **64**: 3927–3948.
Yuter SE, Houze Jr RA. 1995. Three-dimensional kinematic and microphysical evolution of Florida cumulonimbus. Part II: Frequency distributions of vertical velocity, reflectivity, and differential reflectivity. *Mon. Weather Rev.* **123**: 1941–1963.
Zeng X, Tao W-K, Zhang M, Peters-Lidard C, Lang S, Simpson J, Kumar S, Xie S, Eastman JL, Shie C-L, Geiger JV. 2007. Evaluating clouds in long-term cloud-resolving model simulations with observational data. *J. Atmos. Sci.* **64**: 4153–4177.
Zhang D-L, Gao K, Parsons DB. 1989. Numerical simulation of an intense squall line during 10–11 June 1985 PRE-STORM. Part I: Model verification. *Mon. Weather Rev.* **117**: 960–994.
Zhou YP, Tao W-K, Hou AY, Olson WS, Shie C-L, Lau K-M, Chou M-D, Lin X, Grecu M. 2007. Use of high-resolution satellite observations to evaluate cloud and precipitation statistics from cloud-resolving model simulations. Part I: South China Sea Monsoon Experiment. *J. Atmos. Sci.* **64**: 4309–4329.

